



Master Thesis

Frequency-based Substructuring using Scanning Laser Doppler Vibrometry

Paul Maarten Langbroek

June 09, 2025

Supervisors:

Associate Professor, PhD., dr.techn., Jon Juel Thomsen

Assistant Professor, PhD., Marie Brøns

DTU Construct

Department of Civil and Mechanical Engineering

Abstract

Frequency-Based Substructuring is a method used to predict the dynamic behavior of an assembled mechanical system by coupling the frequency response functions of its individual components. Traditionally, vibration responses in Frequency-Based Substructuring are measured using accelerometers. This study explores the feasibility of using a Scanning Laser Doppler Vibrometer as a non-contact alternative. The instrument offers distinct advantages, such as the ability to capture vibration responses across a predetermined grid of points without physically contacting the structure.

The thesis includes both a numerical simulation and a physical experiment, comparing the coupled frequency response functions of a benchmark structure (obtained via Frequency-Based Substructuring) to the reference. Results from the simulation demonstrate strong agreement between the coupled system and the reference. The physical experiment also shows good agreement, even though it is slightly lower. This discrepancy is primarily attributed to the excitation method (a piezoelectric actuator), which is just as critical as the measurement technique for obtaining accurate vibration data.

Contents

1	Introduction	4
2	Dynamic Substructuring.....	8
2.1	The Concept of Frequency-based Substructuring	9
2.2	Basic Example Illustrating Frequency-based Substructuring Coupling.....	11
2.3	Subsystem Coupling by Virtual Point Transformation	16
2.3.1	Deriving the Response Transformation Matrix	19
2.3.2	Deriving the Force Transformation Matrix	20
2.3.3	Relating the Virtual Admittance to the Uncoupled Admittance	21
3	Experiment 1: Simulated Numerical Experiment.....	24
3.1	Experimental Framework	24
3.1.1	Flowchart of the Experimental Process.....	27
3.2	Results of Experiment 1	30
3.2.1	Modal Properties: Natural Frequencies and Mode Shapes	30
3.2.2	Overlaid Numerical FRFs of All Force-Response DoF Combinations.....	31
3.2.3	Numerical FRF Comparison: LM-FBS Coupled vs. Reference	32
4	Experiment 2: Scanning Laser Doppler Vibrometry Experiment	34
4.1	Experimental Framework	34
4.1.1	Technology of SLDV and its Application in Experimental Substructuring	35
4.1.2	Vibration Excitation Method.....	37
4.1.3	Experimental Setup	39
4.1.4	Flowchart of Experimental Data Generation and Processing	41
4.2	Results of Experiment 2	46
4.2.1	Measurement Signal Coherence.....	47
4.2.2	Modal Properties: Natural Frequencies, Damping Ratios, and Mode Shapes	48
4.2.3	Overlaid Experimental FRFs of All Force-Response DoF Combinations	49
4.2.4	Experimental FRF Comparison: LM-FBS coupled vs. Reference.....	50

5 Discussion	52
5.1 Discussion of Experiment 1 (Simulated Numerical Experiment)	52
5.2 Discussion of Experiment 2 (SLDV Experiment).....	56
5.3 Experiment 1 vs. Experiment 2	59
5.4 Applicability of SLDV in FBS.....	61
5.4.1 Strengths of the Experimental Framework for Experiment 2	61
5.4.2 Limitations of the Experimental Framework for Experiment 2	62
6 Conclusion.....	64
6.1 Summary of Main Findings.....	64
6.2 Suggestions for Future Work	65
7 References	66

Acronyms

DoF	Degree of Freedom
DS	Dynamic Substructuring
EMPC	Equivalent Multi-Point Connection
FBS	Frequency-Based Substructuring
FEM	Finite Element Method
FRF	Frequency Response Function
IDM	Interface Deformation Mode
LM-FBS	Lagrange Multiplier FBS
LDV	Laser Doppler Vibrometer / Vibrometry
SLDV	Scanning Laser Doppler Vibrometer /Vibrometry
VP	Virtual Point
VPT	Virtual Point Transformation

1 Introduction

Frequency-Based Substructuring (FBS) is a practical method for predicting the dynamic behavior of an assembled mechanical system by coupling the frequency response functions (FRFs) of its individual components. This process relies on accurate FRFs, which in turn depend on precise and reliable data acquisition. Accelerometers are traditionally used to collect experimental vibration data for FBS. While these sensors are widespread and offer many advantages, they are considered intrusive because attaching them to a structure alters the dynamic behavior. Consequently, the accuracy of the data collected for dynamic analyses is impaired. To overcome such limitations, this thesis investigates an alternative approach for FBS: Scanning Laser Doppler Vibrometry (SLDV). Unlike accelerometers, SLDV is a non-intrusive measurement technique that employs a laser to scan the surface and capture full-field vibration data without impacting the structure's dynamics. The research will evaluate the applicability of SLDV in FBS and explore its potential advantages over accelerometer-based measurements.

Dynamic Substructuring (DS) is a modular approach to structural dynamic systems, which can be analyzed in physical, modal or frequency domains. This study focuses on frequency domain substructuring methods, which offer advantages over modal and, especially, physical domain modeling in experimental environments. In the physical domain, it is impossible to obtain a complete experimental description of a structure, while in the modal domain, high damping or complex frequency behaviors pose significant challenges. Frequency domain methods like FBS can provide accurate results in such challenging experimental settings [1]. These methods characterize structures using their FRFs, which describe dynamic behavior as the linear ratio of responses (outputs) and excitations (inputs).

DS in the frequency domain is also being referred to as Frequency-Based Substructuring (FBS). In general, FBS can predict an assembly's frequency response by coupling the measured or simulated FRFs of its individual subsystems. Regardless of the coupling technique, two conditions must always be fulfilled in FBS [1]:

1. Compatibility condition: Establishes the compatibility of displacements at the common interface.
2. Equilibrium condition: Establishes the equilibrium of forces at the common interface.

In a discretized system, these boundary conditions are easily enforced by coupling displacements and forces at each collocated interface node [2]. In real structures however, such a collocation does not exist, and different solutions have to be considered, one of which is the virtual point transformation (VPT). The VPT is based on the coupling of multiple translational responses close to the interface and projecting them into one common subspace under the rigidity assumption [2]. In this way, rotational degrees of freedom (DoFs) are implicitly accounted for¹, making the VPT a widely-used method for experimental coupling.

In both academic and industrial settings, experiments require significantly more time and resources than numerical simulations or digital models. Therefore, minimizing the number or scope of experiments is always a key objective. One major advantage of FBS is that it allows for re-measurement or simulation of only the replaced component, instead of the entire system. The part can then be coupled with the main system again, no matter if it consists of experimentally or numerically generated data. The benefits of this approach are evident in industrial applications where noise and vibration reduction are critical, allowing for fewer experiments and reduced costs.

A successful application of FBS techniques depends on an accurate data generation method. Classically, 3D piezo accelerometers are used for experimental response measurement due to their advantages such as wide variety of sensor types, simple mounting and operation, and a broad dynamic and frequency range [3]. Despite their advantages, accelerometers have certain limitations. Any physical attachment to a structure alters its dynamic properties, causing each accelerometer to bias the measured response. This effect is particularly significant in experiments involving lightweight structures [4]. Given the additional drawbacks of accelerometers [3], laser technology offers a non-intrusive alternative to these physically attached sensors.

In a recent study², Trainotti et al. [3] investigated the applicability of laser technology for experimental LM-FBS coupling, including the VPT. Using a laser Doppler vibrometry (LDV) instrument, the study highlighted the potential of non-intrusive vibration measurement techniques, as the LDV responses closely matched the accelerometer measurements and the

¹ Directly measuring rotational acceleration is not common in practice since it is more difficult than measuring translational responses [32].

² As of 2025.

validation. In fact, the LDV instrument proved to be more accurate over a broader frequency range than the accelerometers, leading to a strong recommendation for using LDV technology in FBS.

Given the promising findings of LDV, this thesis will conduct further analysis on the potential of laser technology in FBS using a scanning laser Doppler vibrometer (SLDV). The key difference between LDV and SLDV is that an SLDV scans an oscillating surface automatically over a predetermined grid of points. Therefore, the device allows for the recording of full-field surface vibration data, with the level of detail determined by the grid resolution. This is particularly beneficial for FBS coupling because multiple response measurements can be captured simultaneously, saving significant time. Additionally, with the right software, mode shapes can be efficiently estimated after measuring a fine laser grid over the entire surface of the structure in a single pass.

However, since the SLDV scanning process is not instantaneous, classical modal hammer excitation is unsuitable because it would require many repeated hammer hits during the scanning process. Hence, a new experimental setup must be designed that uses a continuous excitation method, such as a piezoelectric actuator. In addition, unlike accelerometers, the SLDV measures vibrations only perpendicular to the surface – yet another technical challenge that must be addressed.

This thesis represents a first investigation into the applicability of SLDV in FBS. Its practical part comprises a physical and a simulated numerical experiment on a two-component benchmark structure:

- Experiment 1: Simulated numerical experiment with FBS coupling, including a reference experiment on the assembled structure.
- Experiment 2: SLDV experiment with FBS coupling, including a reference experiment on the assembled structure.

As the first study of its kind, the discussion section will specifically document both practical and data-processing challenges encountered during the project. This will assist future researchers working with SLDV-based FBS in identifying and overcoming similar challenges.

The thesis will be organized according to the following structure: Chapter 2 provides a literature review of FBS and VPT, placing the SLDV outcomes within a wider context. Furthermore, a

basic 1D example helps to illustrate fundamental FBS theory to readers new to the field. Chapters 3 and 4 present the simulated numerical and SLDV experiments, respectively, outlining experimental preparation, procedure, and results. Chapter 5 discusses the results, compares the numerical and experimental studies, and summarizes the strengths and weaknesses of SLDV technology in FBS. Finally, chapter 6 will conclude on the key findings and propose opportunities for further analysis in the field.

2 Dynamic Substructuring

This section begins with an overview of dynamic substructuring (DS), followed by a detailed presentation of FBS, a subcategory within the broader DS framework [1].

DS is a method in structural dynamics where a system is divided into subsystems, which are analyzed separately before being reassembled to determine the overall dynamic behavior. De Klerk et al. [1] published their “*General Framework for Dynamic Substructuring*” in 2008, which serves as an important benchmark publication for modern dynamic substructuring research. In the publication, substructuring methods are characterized into three domains: the physical, modal, and frequency domains, each containing the same information in theory, given assumptions of linearity [1].

In the physical domain, structures are specified in a discretized system by their stiffness, damping and mass matrices. Coupling subsystems in the physical domain is equivalent to finite element assembly, where individual element matrices are combined. In experimental settings, working with a discretized system is challenging because a complete experimental description cannot be obtained [1], e.g. a stiffness matrix cannot be measured.

The modal domain represents a structure's dynamic reaction by combining its modal responses. That is, the structure's mass, stiffness and damping matrices are transformed into a modal representation – marked by the eigenvectors obtained from solving the system's eigenvalue problem. Although coupling structures in the modal domain (named CMS - component-mode synthesis) is experimentally applicable, it requires distinct circumstances (e.g. uniform frequency behavior or minimal damping) to yield accurate results [1].

In the frequency domain, structures are characterized by its FRFs, which define their dynamic behavior based on the ratio of response to excitation input. The domain is traditionally used when the dynamic properties of subsystems are determined experimentally, as FRFs can be measured directly [1][5]. Since this thesis evaluates the suitability of a new measurement data type for dynamic substructuring from a frequency perspective, the frequency domain is an appropriate framework.

2.1 The Concept of Frequency-based Substructuring

The frequency-based formulation of DS is denoted as Frequency-Based Substructuring (FBS). FBS predicts an assembled system's frequency response by coupling the measured or simulated FRFs of its individual subsystems. For clarity, “coupling” refers to assembling subsystems using a set of boundary conditions.

Several FBS variants can be found in literature, the so-called “primal” assembly approach was formulated by Jetmundsen et al. [6] in 1988 and serves as the theoretical foundation for many further developments in the field. One of those developments is commonly referred to as “Lagrange Multiplier-FBS” (LM-FBS) coupling, the so-called “dual” assembly approach. The method was published in 2006 by de Klerk et al. [7] and presents a simplified reformulation of the findings by Jetmundsen et al. [6], which is why it is often used in modern FBS research [5][8][9][10]. This thesis utilizes the LM-FBS coupling method as outlined in de Klerk et al. [7], which also serves as the basis for the following theoretical presentation of the FBS concept.

The equation of motion of a subsystem s in the time domain provides insight into its dynamic behavior:

$$\mathbf{M}^{(s)} \ddot{\mathbf{u}}(t)^{(s)} + \mathbf{C}^{(s)} \dot{\mathbf{u}}(t)^{(s)} + \mathbf{K}^{(s)} \mathbf{u}(t)^{(s)} = \mathbf{f}(t)^{(s)}, \quad (1)$$

where $\mathbf{f}^{(s)}$ are the time-dependent forces, $\mathbf{u}^{(s)}$ are the time-dependent responses³, and $\mathbf{M}^{(s)}$, $\mathbf{C}^{(s)}$, $\mathbf{K}^{(s)}$ are the mass, damping and stiffness matrices of the subsystem s respectively.

By applying a Fourier transform⁴, the equation of motion can be presented in the frequency domain:

$$[-\omega^2 \mathbf{M}^{(s)} + j\omega \mathbf{C}^{(s)} + \mathbf{K}^{(s)}] \mathbf{U}(\omega)^{(s)} = \mathbf{F}(\omega)^{(s)}, \quad (2)$$

where ω is the angular velocity and $j = \sqrt{-1}$ is the imaginary unit. Uppercase matrices represent their lowercase counterparts in the frequency domain. Rewriting Eq. 2 yields:

$$\mathbf{Z}(\omega)^{(s)} \mathbf{U}(\omega)^{(s)} = \mathbf{F}(\omega)^{(s)}, \quad (3)$$

³ In practice, a response can have various dimensions, such as displacement, velocity, or acceleration.

⁴ Thus assuming linearity since the Fourier transform is linear.

where

$$\mathbf{Z}(\omega)^{(s)} = [-\omega^2 \mathbf{M}^{(s)} + j\omega \mathbf{C}^{(s)} + \mathbf{K}^{(s)}], \quad (4)$$

also called the dynamic stiffness matrix or impedance matrix, contains the subsystem's mass, stiffness, and damping information. Eq. 4 shows the direct harmonic method for FRF synthetization [11]. Eq. 3 can be rewritten:

$$\mathbf{U}(\omega)^{(s)} = \mathbf{F}(\omega)^{(s)} \mathbf{Y}(\omega)^{(s)}, \quad (5)$$

$\mathbf{Y}^{(s)}$ being the admittance matrix of the subsystem s . The admittance contains the FRFs of all DoFs and is the inverse of the impedance matrix $\mathbf{Z}^{(s)}$. It should be emphasized that Eq. 5 represents the equation of motion for a single subsystem without coupling, which is why there are no interface forces included.

From now on, the derivations are based on two subsystems to be coupled, with the frequency dependance (ω) omitted for better readability. Eq. 5 can be rewritten so that it represents the equation of motion for the uncoupled system:

$$\mathbf{U} = \mathbf{Y} (\mathbf{F} + \mathbf{G}), \quad (6)$$

where \mathbf{U} , \mathbf{F} and \mathbf{G} represent responses, internal forces, and interface forces, respectively. Note that \mathbf{U} contains internal and interface responses. The interface forces contain the forces that keep the subsystems together, e.g. the forces within a bolt that connects the subsystems. \mathbf{Y} stands for the admittance matrix of the uncoupled system, comprising the individual admittances of both subsystems, arranged in a block-diagonal form [2].

There are two main boundary conditions incorporated in FBS, the first one being the compatibility condition. It ensures the compatibility of displacements at the common boundary of two subsystems. The signed Boolean constraint matrix \mathbf{B} enforces this by equating the corresponding DoFs along the interface:

$$\mathbf{B}\mathbf{U} = \mathbf{0}. \quad (7)$$

The second boundary condition ensures the equilibrium of forces between corresponding interface DoFs, resulting from Newton's third law [9]:

$$\mathbf{G} = -\mathbf{B}^T \boldsymbol{\lambda}, \quad (8)$$

with $\boldsymbol{\lambda}$ representing Lagrange multipliers – the intensities of the interface forces [9]. Implemented in Eq. 6, it yields

$$\mathbf{U} = \mathbf{Y}(\mathbf{F} - \mathbf{B}^T \boldsymbol{\lambda}). \quad (9)$$

Eq. 7 and Eq. 9 can be seen as a system of equations:

$$\begin{cases} \mathbf{B}\mathbf{U} = \mathbf{0} \\ \mathbf{U} = \mathbf{Y}(\mathbf{F} - \mathbf{B}^T \boldsymbol{\lambda}) \end{cases} \quad (10)$$

Solving Eq. 10 for $\boldsymbol{\lambda}$:

$$\begin{aligned} \mathbf{B}\mathbf{Y}(\mathbf{F} - \mathbf{B}^T \boldsymbol{\lambda}) &= \mathbf{0}, \\ \mathbf{B}\mathbf{Y}\mathbf{F} &= \mathbf{B}\mathbf{Y}\mathbf{B}^T \boldsymbol{\lambda}, \\ \boldsymbol{\lambda} &= (\mathbf{B}\mathbf{Y}\mathbf{B}^T)^{-1} \mathbf{B}\mathbf{Y}\mathbf{F}. \end{aligned} \quad (11)$$

Eliminating $\boldsymbol{\lambda}$ by substituting it back into Eq. 9 yields the final admittance matrix $\mathbf{Y}_{\text{coupled}}$ of the coupled system:

$$\begin{aligned} \mathbf{U} &= \mathbf{Y}\mathbf{F} - \mathbf{Y}\mathbf{B}^T(\mathbf{B}\mathbf{Y}\mathbf{B}^T)^{-1}\mathbf{B}\mathbf{Y}\mathbf{F}, \\ \frac{\mathbf{U}}{\mathbf{F}} &= \mathbf{Y}_{\text{coupled}} = \mathbf{Y} - \mathbf{Y}\mathbf{B}^T(\mathbf{B}\mathbf{Y}\mathbf{B}^T)^{-1}\mathbf{B}\mathbf{Y}. \end{aligned} \quad (12)$$

In Eq. 12, all combinations of FRFs of the assembled system are included; hence, desired FRFs can be visualized⁵. $\mathbf{Y}_{\text{coupled}}$ contains the information about the interface DoFs as many times as there are subsystems – the duplicates may be removed when deemed necessary.

2.2 Basic Example Illustrating Frequency-Based Substructuring Coupling

The theoretical concept of FBS (dual approach) outlined in the previous section will now be applied in a basic example to illustrate its implementation. In the example, the objective is to

⁵ Whenever a specific FRF is plotted, specific input (force) DoF and output (response) DoFs are chosen.

couple two subsystems, a and b, with LM-FBS. For simplicity, all components of a and b are modeled as point masses with a single horizontal DoF, see Figure 1.

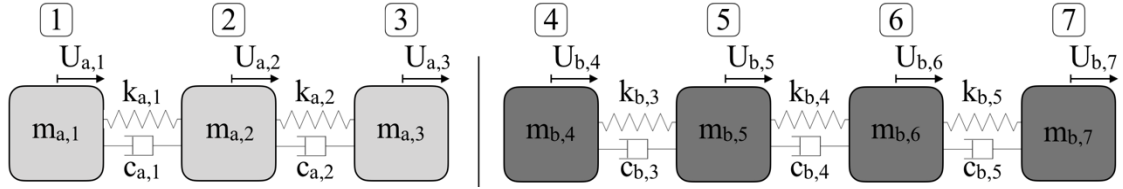


Figure 1: Illustrative subsystems a and b containing:
masses $m_{a,1}, m_{a,2}, m_{a,3}, m_{b,4}, m_{b,5}, m_{b,6}, m_{b,7}$ (1, 2, 3, 2, 4, 1, 5 kg resp.); stiffnesses $k_{a,1}, k_{a,2}, k_{b,1}, k_{b,2}, k_{b,3}$ (100, 200, 50, 400, 200 kg/s² resp.); damping $c_{a,1}, c_{a,2}, c_{b,1}, c_{b,2}, c_{b,3}$ (0.5, 1, 0.25, 2, 1 kg/s resp.).

The coupling procedure usually requires the admittance matrices of the individual subsystems a and b as a starting point. For the example in this chapter, the individual admittances are assumed to be given and defined as \mathbf{Y}^a and \mathbf{Y}^b respectively. The intended coupling configuration can be seen in Figure 2, where the second ($m_{a,2}$) and third ($m_{a,3}$) DoFs of a are collocated with the first ($m_{b,4}$) and second ($m_{b,5}$) DoFs of b.

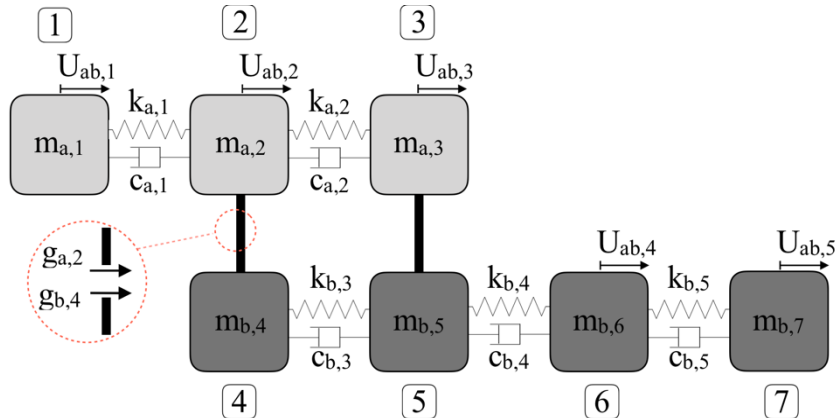


Figure 2: Coupling configuration for subsystems a and b. The black bars indicate the coupling positions and stand for rigid connections. The red detail illustrates the interface forces.

The responses \mathbf{U}^6 , internal forces \mathbf{F} , interface forces \mathbf{G} and the uncoupled admittance matrix $\mathbf{Y}^{a|b}$ are shown in the equation of motion for the uncoupled system in Eq. 13 (corresponding to Eq. 6 of chapter 2.1). As the uncoupled admittance $\mathbf{Y}^{a|b}$ (comprising the individual admittances \mathbf{Y}^a and \mathbf{Y}^b) is a matrix of block-diagonal form⁷, it shows that the subsystems are uncoupled at

⁶ In this example, \mathbf{U} represents displacement, containing internal and interface displacements.

⁷ See Eq. 13: \mathbf{Y}^a is positioned at the top left, while \mathbf{Y}^b is at the bottom right of $\mathbf{Y}^{a|b}$.

this point. Note the separate handling of internal and interface DoFs: in this example, DoFs 1, 6 and 7 are internal, while DoFs 2, 3, 4 and 5 are interface DoFs. That is, G_1^a, G_6^b, G_7^b will eventually be zero, as will $F_2^a, F_3^a, F_4^b, F_5^b$, once the internal DoFs are fully defined away from the interface.

$$\begin{bmatrix} U_1^a \\ U_2^a \\ U_3^a \\ U_4^b \\ U_5^b \\ U_6^b \\ U_7^b \end{bmatrix} = \begin{bmatrix} Y_{11}^a & Y_{12}^a & Y_{13}^a & 0 & 0 & 0 & 0 \\ Y_{21}^a & Y_{22}^a & Y_{23}^a & 0 & 0 & 0 & 0 \\ Y_{31}^a & Y_{32}^a & Y_{33}^a & 0 & 0 & 0 & 0 \\ 0 & 0 & 0 & Y_{44}^b & Y_{45}^b & Y_{46}^b & Y_{47}^b \\ 0 & 0 & 0 & Y_{54}^b & Y_{55}^b & Y_{56}^b & Y_{57}^b \\ 0 & 0 & 0 & Y_{64}^b & Y_{65}^b & Y_{66}^b & Y_{67}^b \\ 0 & 0 & 0 & Y_{74}^b & Y_{75}^b & Y_{76}^b & Y_{77}^b \end{bmatrix} * \begin{pmatrix} F_1^a \\ F_2^a \\ F_3^a \\ F_4^b \\ F_5^b \\ F_6^b \\ F_7^b \end{pmatrix} + \begin{pmatrix} G_1^a \\ G_2^a \\ G_3^a \\ G_4^b \\ G_5^b \\ G_6^b \\ G_7^b \end{pmatrix} \quad (13)$$

The first FBS boundary condition can now be introduced, which ensures the compatibility of displacements at the common interface. The rigid connections (black bars) in Figure 2 symbolically enforce equal horizontal displacements on the coupled DoFs; thus DoFs 2 and 3 (subsystem a) are to be coupled to DoFs 4 and 5 (subsystem b) respectively. The correct interface matching is achieved using the signed Boolean matrix \mathbf{B} : it has as many rows as there are pairs of DoFs to be collocated and as many columns as there are DoFs in the system. As there are seven DoFs in both systems in total and two pairs of DoFs to be collocated, \mathbf{B} is of shape (2,7). The interface DoFs where the displacements must be the same are indicated below:

$$U_2^a = U_4^b \Rightarrow U_4^b - U_2^a = 0, \quad U_3^a = U_5^b \Rightarrow U_5^b - U_3^a = 0. \quad (14)$$

Now, \mathbf{B} can be assembled according to the compatibility condition stated in Eq. 7:

$$\begin{bmatrix} 0 & -1 & 0 & 1 & 0 & 0 & 0 \\ 0 & 0 & -1 & 0 & 1 & 0 & 0 \end{bmatrix} * \begin{bmatrix} U_1^a \\ U_2^a \\ U_3^a \\ U_4^b \\ U_5^b \\ U_6^b \\ U_7^b \end{bmatrix} = \begin{bmatrix} U_4^b - U_2^a \\ U_5^b - U_3^a \end{bmatrix} = 0. \quad (15)$$

Now that displacement compatibility is ensured, the second boundary condition ensures the equilibrium of forces between corresponding interface DoFs. This is based on *actio et reactio*, Newton's third law [9], i.e. for every force, there must be a counterforce with the same

magnitude and opposite direction. Having two pairs of interface DoFs in the example, two conditions can be stated in Eq. 16, considering the equilibrium of interface forces:

$$G_2^a - G_4^b = 0; \quad G_3^a - G_5^b = 0. \quad (16)$$

B can be utilized to substitute **G** by a set of Lagrange multipliers λ , which represent the intensity of the interface forces. Equilibrium must be enforced to both interfaces, therefore, the vector λ is of shape (2,1) [11].

$$\lambda = \begin{bmatrix} \lambda_1 \\ \lambda_2 \end{bmatrix} \quad (17)$$

Hence, the equilibrium conditions can be denoted as:

$$-\mathbf{B}^T \lambda = \mathbf{G} \Rightarrow -\begin{bmatrix} 0 & 0 \\ 0 & -1 \\ -1 & 0 \\ 0 & 1 \\ 1 & 0 \\ 0 & 0 \\ 0 & 0 \end{bmatrix} \begin{bmatrix} \lambda_1 \\ \lambda_2 \end{bmatrix} = \begin{bmatrix} 0 \\ \lambda_2 \\ \lambda_1 \\ -\lambda_2 \\ -\lambda_1 \\ 0 \\ 0 \end{bmatrix} = \begin{bmatrix} G_1^a \\ G_2^a \\ G_3^a \\ G_4^b \\ G_5^b \\ G_6^b \\ G_7^b \end{bmatrix}. \quad (18)$$

The nonzero interface forces (G_1^a, G_6^b, G_7^b are 0, see Eq. 18.) $G_2^a, G_3^a, G_4^b, G_5^b$ are inserted in Eq. 13, which yields (corresponding to Eq. 9):

$$\begin{bmatrix} U_1^a \\ U_2^a \\ U_3^a \\ U_4^b \\ U_5^b \\ U_6^b \\ U_7^b \end{bmatrix} = \begin{bmatrix} Y_{11}^a & Y_{12}^a & Y_{13}^a & 0 & 0 & 0 & 0 \\ Y_{21}^a & Y_{22}^a & Y_{23}^a & 0 & 0 & 0 & 0 \\ Y_{31}^a & Y_{32}^a & Y_{33}^a & 0 & 0 & 0 & 0 \\ 0 & 0 & 0 & Y_{44}^b & Y_{45}^b & Y_{46}^b & Y_{46}^b \\ 0 & 0 & 0 & Y_{54}^b & Y_{55}^b & Y_{56}^b & Y_{57}^b \\ 0 & 0 & 0 & Y_{64}^b & Y_{65}^b & Y_{66}^b & Y_{67}^b \\ 0 & 0 & 0 & Y_{74}^b & Y_{75}^b & Y_{76}^b & Y_{77}^b \end{bmatrix} * \left(\begin{bmatrix} F_1^a \\ F_2^a \\ F_3^a \\ F_4^b \\ F_5^b \\ F_6^b \\ F_7^b \end{bmatrix} + \begin{bmatrix} 0 \\ \lambda_2 \\ \lambda_1 \\ -\lambda_2 \\ -\lambda_1 \\ 0 \\ 0 \end{bmatrix} \right). \quad (19)$$

Applying the same mathematical steps as in Eq. 10, 11 and 12 results in the expression for the coupled admittance \mathbf{Y}^{ab} of the structure depicted in Figure 3:

$$\mathbf{Y}^{ab} = \mathbf{Y}^{a|b} - \mathbf{Y}^{a|b} \mathbf{B}^T (\mathbf{B} \mathbf{Y}^{a|b} \mathbf{B}^T)^{-1} \mathbf{B} \mathbf{Y}^{a|b}. \quad (20)$$

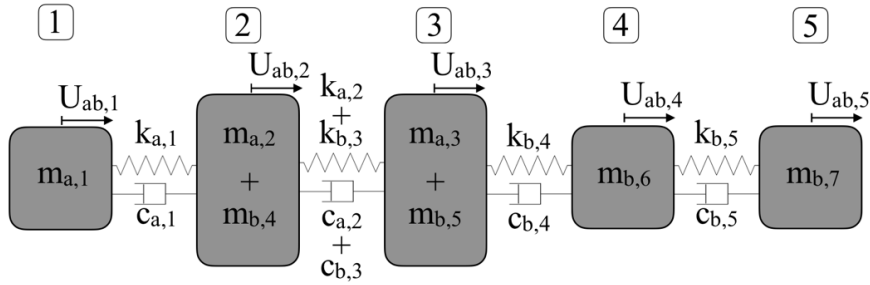


Figure 3: Final coupled structure.

An example FRF of the coupled system is shown in Figure 4, demonstrating successful LM-FBS coupling, as the magnitudes of the coupled and directly synthesized (reference) FRFs are identical. The overlaid FRF of the undamped system highlights damping effects, which are moderate in this case but unavoidable in real-world scenarios. Note that with infinitely fine discretization of the abscissa, the magnitude peaks representing the natural frequencies of the undamped system would become infinitely large. This occurs because an undamped system lacks energy dissipation, leading to infinitely sharp and large resonances. The highest magnitude in Figure 4 represents the rigid body mode which occurs at a frequency close to zero and corresponds to translational motion in the horizontal direction. Rigid body modes do not induce strain within the structure. Note that for a 3D system, rigid body modes correspond to three translations and three rotations [12].

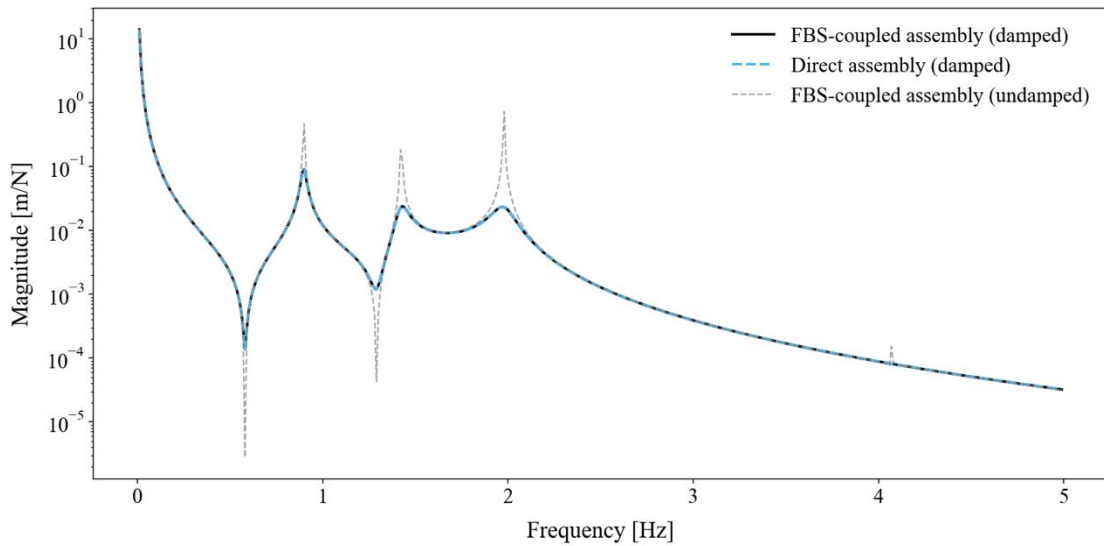


Figure 4: FRF magnitude of the illustrative structure in a 0 to 5 Hz frequency range.
Excitation DoF 1 (input), response DoF 2 (output).

2.3 Subsystem Coupling by Virtual Point Transformation

When the compatibility and equilibrium conditions are satisfied across the interface, FBS yields a perfect coupling result. This was demonstrated in the previous section's example, where each mass was modeled as a point mass and therefore could only be coupled at a single point. Similarly, in discretized FEM models, both FBS boundary conditions can be enforced at every collocated interface node [9], provided that the meshes of both parts align. An example for a discretized coupling arrangement can be seen in the bolted joint illustration in Figure 5.

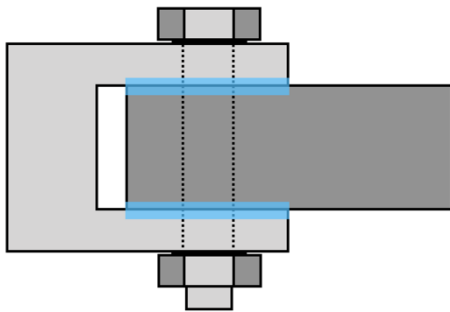


Figure 6: Surface contact.
Redrawn from [2].

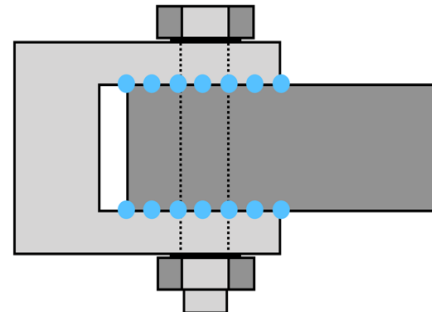


Figure 5: Coupling with discrete FEM nodes. Redrawn from [2].

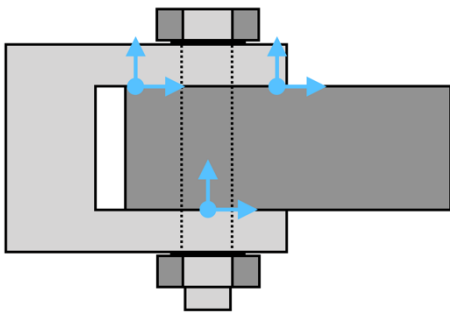


Figure 8: EMPC (translational DoFs only). Redrawn from [2].

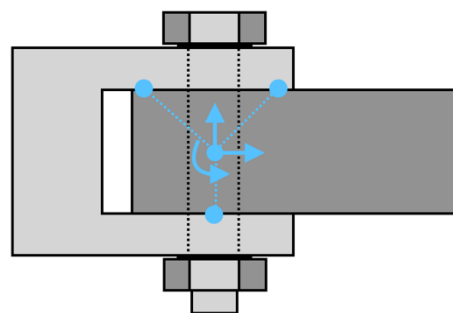


Figure 7: VPT (9 translational DoFs \rightarrow 3 translational & 3 rotational DoFs).
Redrawn from [2].

However, when dealing with continua in experimental settings, a perfect collocation of points or interface nodes cannot be realized. In practice, the interface problem is typically reduced to one or more distinct nodes, as a line or surface contact (common in real mechanical problems, see Figure 6) would require an infinite amount of DoFs [2]. Coupling subsystems by means of a single 3-axial translational single point connection does not account for rotational DoFs. However, coupling multiple of such 3-axial translational points close to the interface implicitly

accounts for rotational DoFs, which is shown in Figure 8. Since 6 DoFs are enough to define movement in 3D space, three 3-axial translational accelerometers (when not in a line) are sufficient to fully determine the coupling of the required three translations and three rotations [2]. The issue with this so called equivalent multi-point connection (EMPC) is that it can overdetermine the interface problem⁸, making it less robust. That is, the two FBS boundary conditions will overcompensate mismatches in movement (caused by experimental errors), which “stiffens” the interface problem, leading to unwanted peaks in the coupled FRF [2].

The virtual point transformation (VPT) provides a solution to this overdetermination of the interface problem by means of interface deformation modes (IDMs). For each interface, only the necessary 6 DoFs (6 IDM) are coupled by projecting the full admittance data – typically 9 DoFs or more – onto a so-called IDM subspace (see Figure 7). By doing so, one merely retains the dynamics that load the interface in a rigid way, which leaves residual flexible motion uncoupled, effectively “weakening” the interface problem⁹ [2]. The IDM subspace corresponds to a virtual point (VP), as no direct measurements are required at this point. In fact, since the VP needs to be in proximity to the interface, the point is often not accessible by measurement equipment. Nevertheless, a coinciding placement of VPs of separate subsystems is possible and desirable [9], making the VPT experimentally applicable.

Although the experimental part of this thesis uses SLDV measurement data, the following VPT derivations will be demonstrated by a simple illustration with translational accelerometers, see Figure 9. For simplicity, we will refer to the accelerometers as sensors and to their outputs simply as responses¹⁰.

⁸ 9 DoFs are coupled while only 6 DoFs are necessary to fully define the movement.

⁹ Possible measurement errors are averaged out by least-squares reduction.

¹⁰ In FBS literature (e.g. [3] or [13]), sensor responses are often referred to as displacements for simplicity, even though the sensors typically measure translational acceleration.

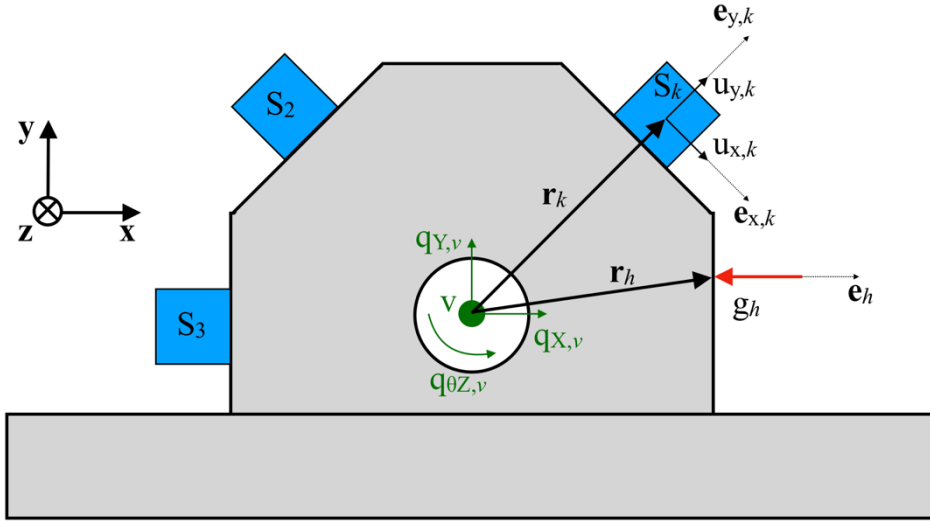


Figure 9: A subsystem's interface to be coupled via VPT.
 Blue: k triaxial translational accelerometers; red: interface forces;
 green: VP v and its DoFs. Drawing inspired by [2].

It is important to emphasize that the VPT is conducted separately for each coupling interface of each subsystem (a subsystem can have multiple coupling interfaces – and thus multiple VPs), eventually yielding a distinct virtual admittance \mathbf{Y}_{qm} for each VP of each subsystem:

$$\mathbf{Y}_{qm} = \mathbf{T}_u \mathbf{Y}_{mea} \mathbf{T}_g^T. \quad (21)$$

Subscript qm refers to the virtual (the VP's) responses \mathbf{q} and virtual forces & moments \mathbf{m} , see sections 2.3.1 and 2.3.2. Although \mathbf{Y}_{qm} is determined separately, the subsystems to be coupled must have perfectly collocated VPs, with the responses and forces & moments of each VP being perfectly aligned. \mathbf{Y}_{mea} is the measured admittance at a coupling interface. It provides the ratio of responses and forces in proximity to the interface (\mathbf{u} and \mathbf{g} , shown in Figure 9). These responses and forces are projected into the VP by \mathbf{T}_u and \mathbf{T}_g – the transformation matrices for responses and forces. Subscripts u and g refer to the interface responses \mathbf{u} and interface forces \mathbf{g} , respectively, see sections 2.3.1 and 2.3.2.

To fully define Eq. 21, sections 2.3.1 and 2.3.2 focus on deriving expressions for \mathbf{T}_u and \mathbf{T}_g , demonstrated using the example of Figure 9.

2.3.1 Deriving the Response Transformation Matrix

Figure 9 illustrates that the VP v has 6 virtual responses¹¹ $\mathbf{q}_v = [q_{X,v}, q_{Y,v}, q_{Z,v}, q_{\theta X,v}, q_{\theta Y,v}, q_{\theta Z,v}]^T$, where $[q_{X,v}, q_{Y,v}, q_{Z,v}]$ indicate translational, and $[q_{\theta X,v}, q_{\theta Y,v}, q_{\theta Z,v}]$ indicate rotational components. For the sensor k , the interface responses \mathbf{u}_k (typically translational) can be expressed in terms of the virtual responses \mathbf{q}_v of v . Therefore, it is important to identify which motions of v contribute to the interface responses $\mathbf{u}_k = [u_{x,k}, u_{y,k}, u_{z,k}]$ measured by the sensor S_k . Note that subscripts x,y,z define the orientation of the sensor k , while subscripts X,Y,Z form the coordinate system of v . A matrix \mathbf{E}_k can be used to accommodate the discrepancy between the orientation of the sensor channels and v in Figure 9, where $[e_{x,X,k}, e_{x,Y,k}, e_{x,Z,k}]^T$ is the orientation of the sensor channel x ; the same principle applies to the sensor channels y and z . The distance from the sensor k to v is denoted by $\mathbf{r}_k = [r_{X,k}, r_{Y,k}, r_{Z,k}]$.

The relation between \mathbf{u}_k and \mathbf{q}_v can be expressed as:

$$\begin{bmatrix} u_{x,k} \\ u_{y,k} \\ u_{z,k} \end{bmatrix} = \begin{bmatrix} e_{x,X,k} & e_{x,Y,k} & e_{x,Z,k} \\ e_{y,X,k} & e_{y,Y,k} & e_{y,Z,k} \\ e_{z,X,k} & e_{z,Y,k} & e_{z,Z,k} \end{bmatrix} \begin{bmatrix} 1 & 0 & 0 & 0 & r_{Z,k} & -r_{Y,k} \\ 0 & 1 & 0 & -r_{Z,k} & 0 & r_{X,k} \\ 0 & 0 & 1 & r_{Y,k} & -r_{X,k} & 0 \end{bmatrix} \begin{bmatrix} q_{X,v} \\ q_{Y,v} \\ q_{Z,v} \\ q_{\theta X,v} \\ q_{\theta Y,v} \\ q_{\theta Z,v} \end{bmatrix}, \quad (22)$$

or, in compact matrix notation:

$$\mathbf{u}_k = \mathbf{E}_k \check{\mathbf{R}}_k \mathbf{q}_v = \mathbf{R}_k \mathbf{q}_v. \quad (23)$$

The $\check{\mathbf{R}}_k$ matrix' columns represent the translations in X, Y, Z (columns 1, 2, 3) and the rotations around X, Y, Z (columns 4, 5, 6).

Eq. 23 describes the relation between \mathbf{u}_k and \mathbf{q}_v (regarding one sensor S_k and one VP v). A more general relation for $h_u = 1 \dots n$ sensor's interface responses \mathbf{u} and $h_q = 1 \dots n$ virtual (for multiple VPs) responses \mathbf{q} can be stated as

$$\mathbf{u} = \mathbf{R} \mathbf{q}, \quad (24)$$

where \mathbf{R} is the matrix formed by stacking the \mathbf{R}_k matrices of all k sensors across all VPs.

¹¹ In a 2D figure, only 2 translations and 1 rotation are illustrated.

Note that \mathbf{q} still contains 6 virtual responses per VP. The projection of the sensor's admittances into the IDM subspace occurs under the rigidity assumption in proximity of v . Since this assumption is not fully valid in reality, a residual $\boldsymbol{\mu}$ will be introduced, representing the remainder of flexibility not captured by the IDM projection [2]:

$$\mathbf{u} = \mathbf{R} \mathbf{q} + \boldsymbol{\mu}. \quad (25)$$

To determine the solution that most closely matches the measured response, a residual cost function ($\boldsymbol{\mu}^T \boldsymbol{\mu}$) must be minimized. One can obtain a solution in a least-squares sense by finding the Moore-Penrose pseudo-inverse of \mathbf{R} ¹²:

$$\mathbf{q} = (\mathbf{R}^T \mathbf{R})^{-1} \mathbf{R}^T \mathbf{u}. \quad (26)$$

Furthermore, a symmetric weighting matrix \mathbf{W} can be introduced that controls the importance of certain DoFs for the transformation [2]:

$$\mathbf{q} = (\mathbf{R}^T \mathbf{W} \mathbf{R})^{-1} \mathbf{R}^T \mathbf{W} \mathbf{u} = \mathbf{T}_u \mathbf{u} \Rightarrow \mathbf{T}_u = (\mathbf{R}^T \mathbf{W} \mathbf{R})^{-1} \mathbf{R}^T \mathbf{W}. \quad (27)$$

The response transformation matrix \mathbf{T}_u projects translational interface responses into an IDM subspace that corresponds to a VP. The influence of the residual flexibility is filtered out from \mathbf{q} [11], preventing an overdetermination of the interface problem.

2.3.2 Deriving the Force Transformation Matrix

The interface forces \mathbf{g} are transformed into the VP v in a similar way as the interface responses \mathbf{u} in the previous section. All interface forces (h -th force g_h illustratively shown in Figure 9) need to be related to the virtual forces & moments $\mathbf{m}_v = [m_{X,v}, m_{Y,v}, m_{Z,v}, m_{\theta X,v}, m_{\theta Y,v}, m_{\theta Z,v}]$ of v , where $[m_{X,v}, m_{Y,v}, m_{Z,v}]$ denote virtual forces, and $[m_{\theta X,v}, m_{\theta Y,v}, m_{\theta Z,v}]$ denote virtual moments. For g_h , this can be done by the relation

$$\begin{bmatrix} m_{X,v} \\ m_{Y,v} \\ m_{Z,v} \\ m_{\theta X,v} \\ m_{\theta Y,v} \\ m_{\theta Z,v} \end{bmatrix} = \begin{bmatrix} 1 & 0 & 0 \\ 0 & 1 & 0 \\ 0 & 0 & 1 \\ 0 & -r_{Z,h} & r_{Y,h} \\ r_{Z,h} & 0 & -r_{X,h} \\ -r_{Y,h} & r_{X,h} & 0 \end{bmatrix} \begin{bmatrix} e_{X,h} \\ e_{Y,h} \\ e_{Z,h} \end{bmatrix} g_h, \quad (28)$$

¹² For a detailed documentation of the pseudo-inverse operation, see [13].

the vector $\mathbf{e}_h = [e_{x,h}, e_{y,h}, e_{z,h}]^T$ denoting the orientation of g_h , and the vector $\mathbf{r}_h = [r_{x,h}, r_{y,h}, r_{z,h}]$ denoting the distance from g_h to v . Eq. 29 shows the compact matrix notation of Eq. 28:

$$\mathbf{m}_v = \tilde{\mathbf{R}}_h^T \mathbf{e}_h \mathbf{g}_h = \mathbf{R}_h^T \mathbf{g}_h. \quad (29)$$

A more general relation for $h_m = 1 \dots n$ virtual (for multiple VPs) forces & moments \mathbf{m} and $h_g = 1 \dots n$ interface forces \mathbf{g} can be stated:

$$\mathbf{m} = \mathbf{R}^T \mathbf{g}. \quad (30)$$

The solution for \mathbf{g} (and ultimately \mathbf{T}_g) cannot be determined in a least-squares sense since the problem is underdetermined. Instead, the solution is found by minimizing a scalar cost function $\mathbf{g}^T \mathbf{g}$, using $\mathbf{R}^T \mathbf{g} - \mathbf{m} = \mathbf{0}$ as a constraint [13]:

$$\mathbf{g} = \mathbf{R}(\mathbf{R}^T \mathbf{R})^{-1} \mathbf{m}. \quad (31)$$

In alignment with section 2.3.1, a symmetric weighting matrix \mathbf{W} can be introduced [2], which yields the expression for the force transformation matrix \mathbf{T}_g :

$$\mathbf{g} = \mathbf{W} \mathbf{R}(\mathbf{R}^T \mathbf{W} \mathbf{R})^{-1} \mathbf{m} = \mathbf{T}_g^T \mathbf{m} \Rightarrow \mathbf{T}_g^T = \mathbf{W} \mathbf{R}(\mathbf{R}^T \mathbf{W} \mathbf{R})^{-1}. \quad (32)$$

Now that \mathbf{T}_g^T and \mathbf{T}_u are fully defined, both matrices can be inserted into Eq. 21, thereby completing the VPT and yielding the transformed virtual admittances

2.3.3 Relating the Virtual Admittance to the Uncoupled Admittance

Once \mathbf{T}_u and \mathbf{T}_g are derived, the virtual admittance \mathbf{Y}_{qm} is fully defined (see Eq. 21) and LM-FBS can be applied. Nevertheless, it is important to illustrate the process of obtaining the uncoupled admittance \mathbf{Y} (corresponds to $\mathbf{Y}^{A|B}$ in section 2.2.) from the virtual admittance \mathbf{Y}_{qm} . This was not addressed in sections 2.1 and 2.2, as both sections focused on FBS with the assumption of perfectly collocated interface DoFs.

Recall that \mathbf{Y} can be visualized as a block matrix, comprising the individual admittances of the subsystems to be coupled. Each individual admittance consists of an internal (away from the interface) component and an interface-related (in proximity to the interface) component. This is demonstrated in Figure 10, which shows the composition of \mathbf{Y} for symbolic subsystems 1

(light grey) and 2 (dark grey). The left illustration shows the composition of \mathbf{Y} before the VPT, and the right illustration shows it after the VPT.

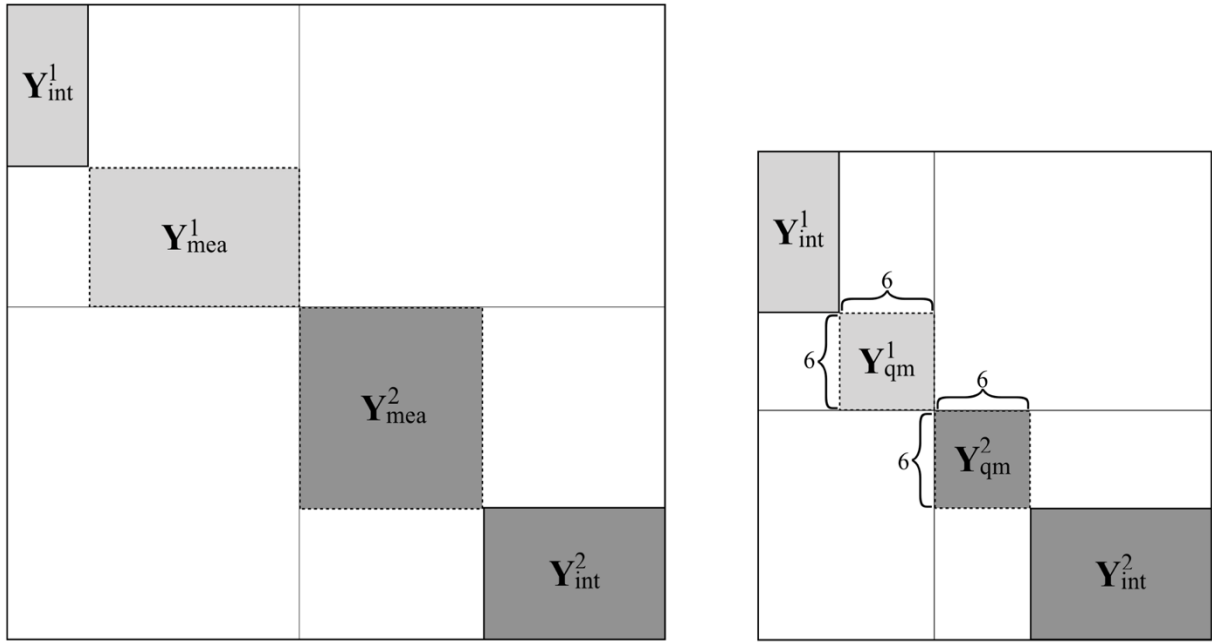


Figure 10: Block matrix visualization for symbolic subsystems 1 and 2, showing the uncoupled admittance \mathbf{Y} before (left) and after (right) a 3D VPT. The internal sub-admittances $\mathbf{Y}_{\text{int}}^1$ and $\mathbf{Y}_{\text{int}}^2$ remain unchanged while the interface sub-admittances $\mathbf{Y}_{\text{mea}}^1$ and $\mathbf{Y}_{\text{mea}}^2$ transform into 6x6 virtual sub-admittances \mathbf{Y}_{qm}^1 and \mathbf{Y}_{qm}^2 .

Before the VPT, the admittances of the symbolic subsystems 1 and 2 each comprise an internal sub-admittance¹³ and an interface sub-admittance¹⁴. The shape of the internal and interface sub-admittances depends on the number of responses and forces chosen away from, and in proximity to the interface, respectively. While the number of DoFs of the internal sub-admittances can be selected freely and is identical before and after the VPT, the interface sub-admittances must have a minimum number of DoFs for proper VPT application. The shape of a transformed virtual admittance \mathbf{Y}_{qm} is always 6x6 for a 3D VPT, reflecting the coupling of 3 translational and 3 rotational DoFs¹⁵, with each DoF corresponding to a row and column in \mathbf{Y}_{qm} .

For a 3D VPT to function mathematically, the minimum number of DoFs for the interface sub-admittances (Figure 10: $\mathbf{Y}_{\text{mea}}^1$ and $\mathbf{Y}_{\text{mea}}^2$) is 6 responses (e.g., 6 accelerometer channels) and 6 forces (e.g., 6 hammer impacts). Nevertheless, a minimum of 9 responses (e.g. 3 accelerometers

¹³ $\mathbf{Y}_{\text{int}}^1$ and $\mathbf{Y}_{\text{int}}^2$; subscript int stands for “internal”.

¹⁴ $\mathbf{Y}_{\text{mea}}^1$ and $\mathbf{Y}_{\text{mea}}^2$; subscript mea stands for “measured”.

¹⁵ In a “1D experiment”, where the FRFs are obtained exclusively along a single direction in space, the dynamics captured are associated with one translational DoF and two out-of-plane rotational DoFs [3]. Such a 1D VPT will be used for the experimental part of this thesis.

with 3 channels each) and 9 forces (e.g. 9 hammer impacts) is typically used in practice, as this ensures that all DoFs of \mathbf{Y}_{qm} are independently accounted for. Furthermore, the effects of noise and misalignment can be confined [9]. A detailed explanation regarding the quantity and placement of the interface responses and forces is provided in [9].

3 Experiment 1: Simulated Numerical Experiment

Experiment 1 is a numerical analysis aimed at determining a suitable configuration of forces and sensors, allowing for quick adjustments before conducting the SLDV experiment (Experiment 2). Furthermore, Experiment 1 demonstrates the performance of the VPT and provides a basis for comparison with the SLDV experiment.

All experiments will be performed on a benchmark structure known as the AM Structure. It is an academic example of a beam-like structure that is used for research in experimental substructuring, e.g. in [14] or [15]. The AM Structure consists of two subsystems A and B (see Figure 11), which can be connected at a specified interface to obtain the assembly shown in Figure 12.

3.1 Experimental Framework

For practical and geometric reasons, the experiments in this thesis are conducted along the Z-direction, which corresponds to the AM structure's main flat surface (see Figure 11 or Figure 12). While vibrations in other directions could theoretically be measured, only the Z-plane provides an entirely flat and easily aligned surface with a broad area for capturing internal DoF responses. Measuring in X or Y would not only require repositioning the SLDV or altering the suspension setup (see e.g., Figure 26), but also complicate the VPT, since the structure's geometry provides only a single interface surface in those directions (e.g., subsystem A in Y, subsystem B in X). These considerations are particularly significant for Experiment 2, where physical testing creates more constraints than the all-at-once numerical simulations of Experiment 1.

Accordingly, Figure 11 and Figure 12 show forces and responses exclusively in Z, and all FRFs in this thesis are synthesized along that axis. With regard to Experiment 2, the arrangement allows all required SLDV measurements for each force position to be captured in a single scan run – minimizing the number of scans and fully leveraging the scanner's capabilities.

Figure 11 illustrates the necessary distinction between internal and interface DoFs. Internal DoFs comprise internal (away from the interface) responses and forces and are used to display the FRFs after coupling by choosing a specific force-response DoF combination. Interface DoFs comprise interface (in proximity to the interface, in accordance with the rigidity assumption) responses and forces and are only used to perform the VPT. Note that the VPT, although capable

of processing 3 translational and 3 rotational DoFs¹⁶, will only account for 1 translational (Z) and 2 rotational (X, Y) DoFs in this study. The rotations in X and Y are implicitly accounted for when the interface DoFs span a surface [9], which is provided in the experimental configuration (see interfaces of A and B in Figure 11). A VP is displayed for both subsystems A and B, as the VPT is applied independently to the interface DoFs of each subsystem.

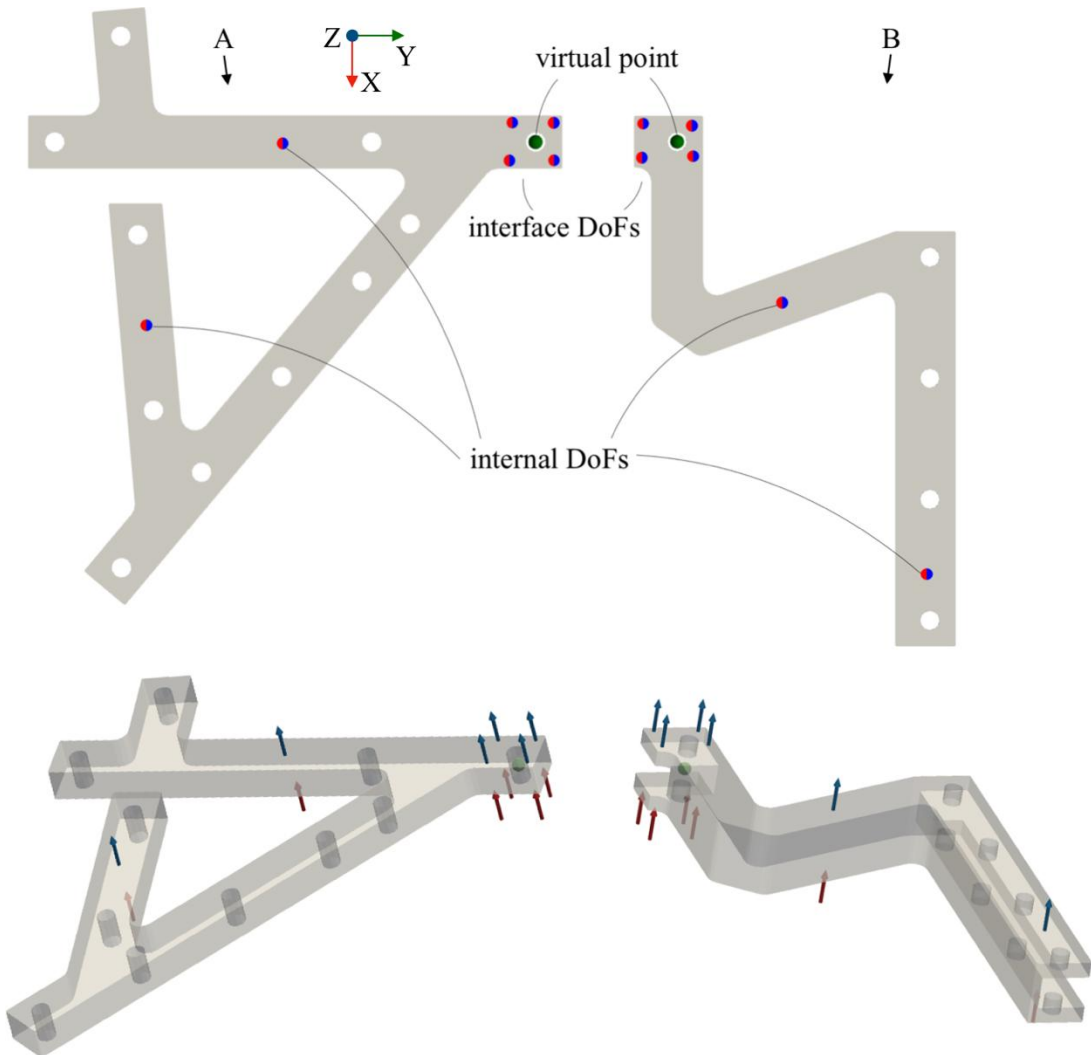


Figure 11: Top and 3D view of subsystems A and B with responses, force, and VP positions. From the top view perspective, the positions of the measurements and forces are congruent (illustrated by “•”). In the 3D view, blue and red arrows denote responses and forces, respectively. The green spheres mark the position of the VP within A and B.

¹⁶ The VPT is usually applied with 3 translations and 3 rotations, using tri-axial accelerometers.

Once the interface DoFs are reduced into the shared IDM subspace (the VP), LM-FBS can be applied. Since A and B are to be connected at the common interface, the reduced virtual DoFs of A and B cancel out according to the FBS compatibility and equilibrium conditions. Hence, the assembly depicted in Figure 12 does not display interface DoFs anymore.

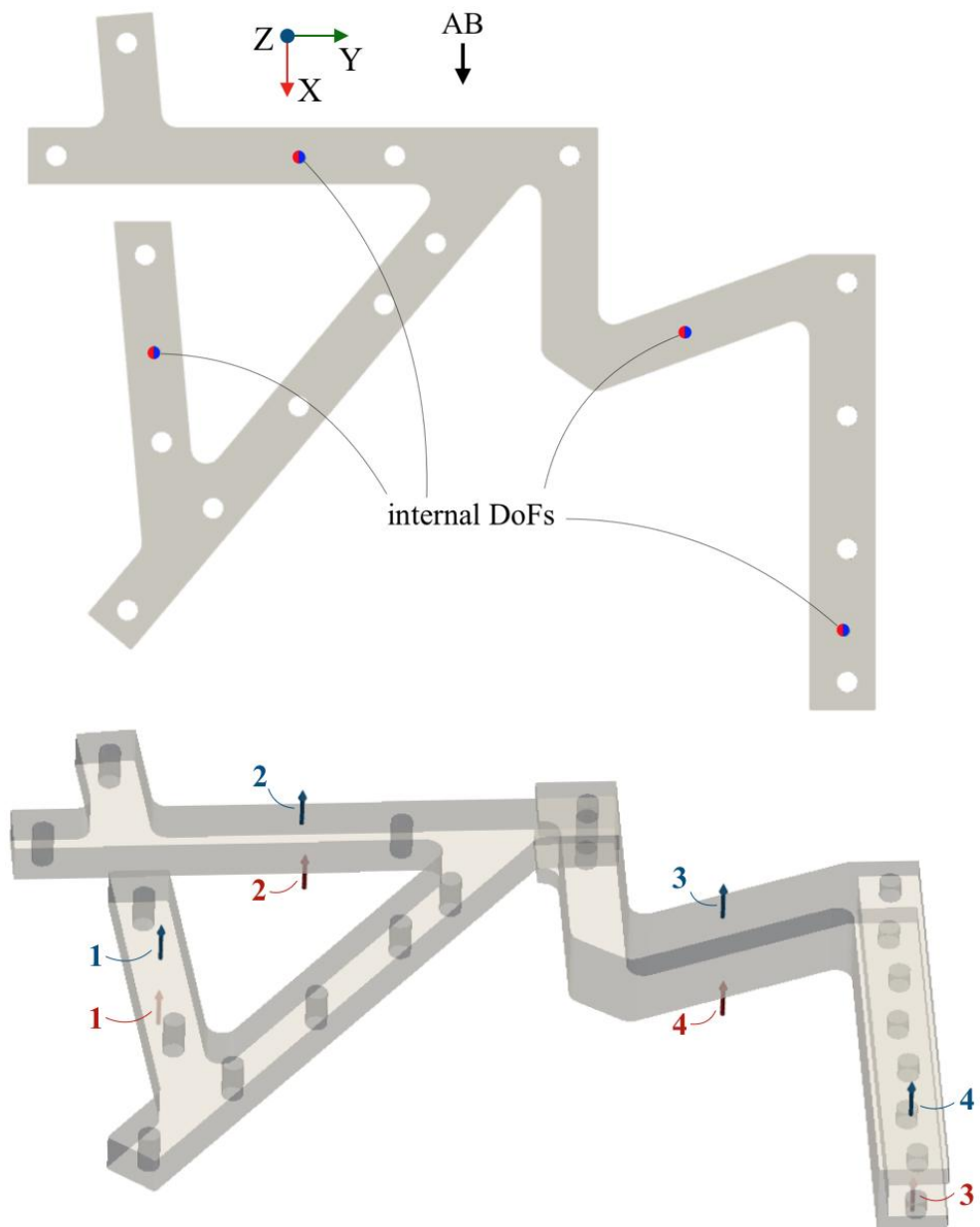


Figure 12: Top and 3D view of the assembled AM structure with internal responses and forces. From the top view perspective, the positions of the responses and forces are congruent (illustrated by “•”). In the 3D view, blue and red arrows denote responses and forces, respectively. The numbers indicate the indexing of forces and responses, which will be referenced when identifying the DoFs chosen for the FRF plots.

3.1.1 Flowchart of the Experimental Process

The simulated numerical experiment involves multiple steps of data generation and processing. Figure 13 provides a comprehensive overview, starting with data preprocessing (steps 1a, 1b, 1c) and ending with FRF analysis (step 6). In contrast to subsystems A and B, the reference FRFs are obtained without FBS; only steps 1a, 1b, 2, 5 and 6 are required.

The FBS computations (outlined in chapter 2) in this thesis are performed with the Python package pyFBS. pyFBS is an open-source Python library that implements state-of-the-art FBS methodologies, like the VPT. It allows both experimental and numerical data to be fed. Furthermore it allows the synthetization of FRFs and the visualization and analysis of components and measurement setups [16].

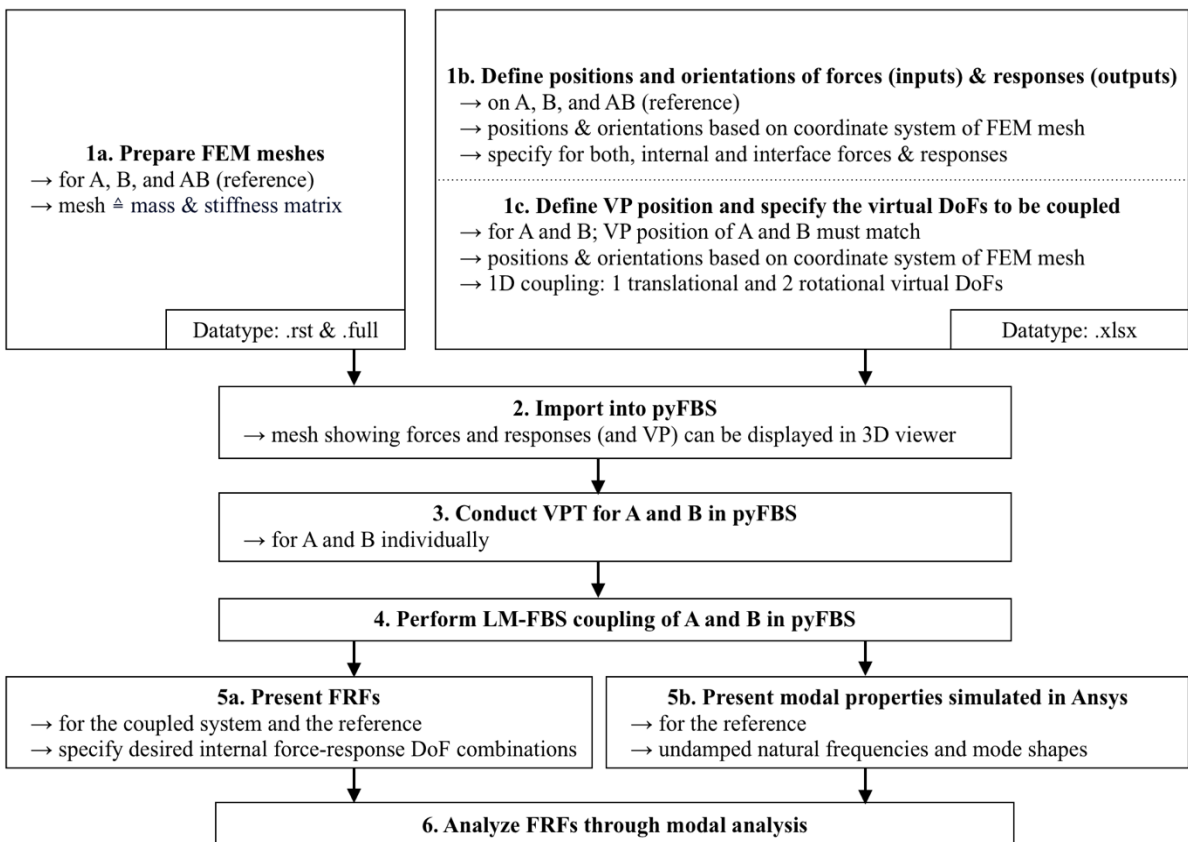


Figure 13: Flowchart of the simulated numerical experiment.

Initially, the FEM meshes for A, B and the reference AB must be prepared (step 1a, Figure 13). This can be done using FEM software; for this project, Ansys Workbench is used. A tetrahedral mesh was chosen for all structures, generated with the patch conforming algorithm and an

element size of 3 mm. A pair of pyFBS-compatible files – namely .rst and .full – can be generated during the meshing process in Ansys. These files contain node locations, DoFs, connectivity, and the mass and stiffness matrices [11]. By default, the .rst and .full files are used only as intermediate files in Ansys and are deleted once meshing is complete. In this project, the files are retained and serve as the FEM data input into pyFBS.

In steps 1b and 1c, the positions and orientations of forces and responses, and the VP, are specified in a pyFBS-compatible Excel document (.xlsx), with the coordinates corresponding to the FEM meshes‘ coordinate systems¹⁷. The document contains worksheets for responses¹⁸, forces, virtual responses, and virtual forces & moments (separate worksheets for every subsystem and the reference). The necessary distinction between internal and interface DoFs is considered in the respective worksheets. The coordinates of virtual responses and virtual forces & moments must agree, as these represent the position of the VP. Furthermore, the virtual responses and virtual forces & moments entered in the Excel document implicitly specify the dimension of the VPT.

In step 2, the FEM meshes, CAD parts (only used for visualization), and the Excel document are imported into pyFBS. Now, responses, forces and the VP can be displayed on the respective meshes or CAD parts in a 3D viewer, as shown in the bottom illustrations of Figure 11 and Figure 12. Note that after import, pyFBS synthesizes the FRFs for A, B, and AB, using the mesh along with the defined force and response DoFs. The FRFs are synthesized assuming light damping (damping ratio $\zeta = 0.3\%$), with the intention of reflecting the behavior of the physical aluminum AM structure used in Experiment 2.

The VPT for A and B is conducted in step 3. Figure 10 shows the effect of a 3D VPT on the uncoupled admittance, resulting in virtual sub-admittances of size 6x6 (3 translational virtual responses, 3 rotational virtual responses, 3 virtual forces, and 3 virtual moments). However, the 1D VPT conducted in this thesis results in virtual sub-admittances of size 3x3. This means that the 4 interface responses and forces on each subsystem’s interface (shown in Figure 11)

¹⁷ pyFBS automatically assigns every set of coordinates specified in the Excel document to the coordinates of the closest node in the FEM mesh.

¹⁸ For every response position, a plurality of channels with arbitrary orientation can be specified. This allows a variety of measurement equipment to be simulated, e.g. tri-axial (3 channels) or unidirectional (1 channel) accelerometers, or an SLDV (1 channel).

transform into 1 translational virtual response, 2 rotational virtual responses, 1 virtual force, and 2 virtual moments.

It is worth explaining how the input data for the pyFBS VPT function (used in both Experiments 1 and 2) is structured. This understanding will be essential for correctly assembling the data generated in Experiment 2 after importing it into pyFBS. Unlike in Experiment 1, where the FRF arrays are obtained in a consolidated manner, in Experiment 2, the FRF arrays are acquired individually for each sub-experiment, which each sub-experiment corresponding to a distinct force position. This difference in data structure between the two experiments requires attention to ensure proper data integration after importing into pyFBS.

The pyFBS built-in function that performs the VPT for A (subsystem A is used for demonstration) is called *VPA.apply_VPT(MK_A.freq, MK_A.FRF)*. *VPA.apply_VPT* is the function name, and *MK_A.freq* and *MK_A.FRF* are the function inputs, representing the frequency array and the synthesized FRF array of A, respectively. Recall that for the VPT, only the interface DoFs are required. Although A has 4 interface forces and responses, the shape of *MK_A.FRF* is (6, 6, 3200), reflecting 6 forces (2 internal, 4 interface) and 6 responses (2 internal, 4 interface) across 3200 data points. While acquiring an FRF with an internal input DoF and an interface output DoF (or vice versa) is redundant, such a force-response DoF combination could theoretically be displayed in the manner pyFBS saves the synthesized FRF arrays. It is therefore important to highlight that the FRF input array to *VPA.apply_VPT* includes all DoFs (internal and interface), although merely the interface DoFs are used in the VPT function¹⁹. The internal DoFs are retained in the function simply to keep all FRF data of A in a single array.

The LM-FBS coupling of subsystems A and B is performed in step 4 using pyFBS. This yields the coupled admittance \mathbf{Y}^{AB} , which provides the dynamic response of every internal output DoF (responses) for every internal input DoF (forces).

Any force-response DoF combination can be visualized through FRFs (can be done in pyFBS) in step 5a. A direct comparison of the coupled system and the reference provides insights into the quality of the VPT. This is particularly interesting in this thesis, since a 1D VPT does not

¹⁹ The pyFBS VPT function *VPA.apply_VPT* can distinguish between internal and interface DoFs based on groupings assigned in the Excel document.

couple all spatial DoFs. Additionally, the reference's mode shapes at its corresponding natural frequencies are displayed in Ansys (step 5b).

In step 6, the shape of specific FRFs can be analyzed using the mode shapes and the position of the selected input and output DoFs.

3.2 Results of Experiment 1

This section presents the results of Experiment 1. First, the modal properties of the assembled AM Structure, obtained from the Ansys model, are shown. Then, overlaid FRFs of all force-response combinations are presented. Overlaid FRFs highlight common resonance peaks across DoFs, helping to identify natural frequencies and providing qualitative insight into mode shape characteristics. They also help visually assess the consistency and quality of the measurements. Finally, a set of chosen FRFs is shown – demonstrating the successful FBS implementation by comparing the LM-FBS coupled AM Structure with the reference. Since visual comparison provides only a qualitative evaluation, average coherence values are included to quantitatively assess the agreement between the FRFs.

3.2.1 Modal Properties: Natural Frequencies and Mode Shapes

The modal properties of the reference are extracted from Ansys, using the same FEM mesh that is imported into pyFBS in step 2 of Figure 13. Once the material parameters are set (see section 4.1 for details), the modal properties can be simulated within the 0 to 2 kHz frequency range in the *Modal* tool of the software. In FEM modeling, modal analysis is typically performed without considering damping, only considering mass and stiffness. The goal is to extract natural frequencies and mode shapes, which are inherent properties of the structure and are calculated assuming undamped free vibration. The simulated mode shapes and undamped natural frequencies f are presented in Figure 14.

Within the framework of Experiment 1, eight undamped natural frequencies and corresponding mode shapes are identified. The majority of the undamped natural frequencies lie in the lower frequency range, with only two out of eight located above 1.1 kHz.

The colors in the mode shape images represent vibration amplitude: blue and turquoise indicate low levels, green and yellow indicate moderate levels, and orange and red indicate high levels.

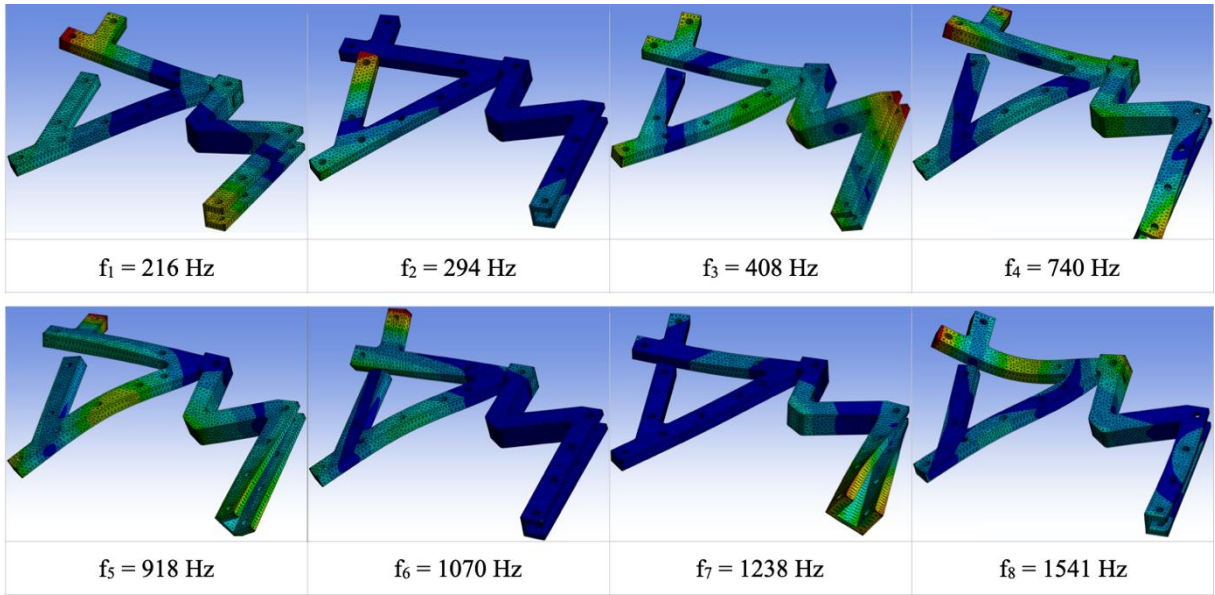


Figure 14: Simulated modal properties of AB, i.e. mode shapes and undamped natural frequencies f . The properties are extracted from Ansys Workbench in the frequency range 0 to 2 kHz.

It is important to note that, in accordance with the experimental framework of this thesis, Figure 14 only presents mode shapes (and natural frequencies) that involve movement in the Z-direction. Additional natural frequencies were identified in the simulation between several of the presented frequencies; however, these correspond to modes without movement in Z. Consequently, the additional frequencies do not appear in the FRFs presented in sections 3.2.2 and 3.2.3, as those FRFs are limited to forces and responses in the Z-direction.

3.2.2 Overlaid Numerical FRFs of All Force-Response DoF Combinations

This section presents the overlaid FRFs for all 16 force-response combinations. Overlaid FRFs examine the presence of common resonance peaks across DoFs, helping to identify natural frequencies and providing qualitative insight into mode shape characteristics. They also help visually assess the consistency and quality of the measurements.

Figure 15 shows the overlaid FRFs for the LM-FBS coupled AM Structure (left plot) and the reference (right plot). Common resonance peaks can be clearly identified between the respective curves. Initial observation reveals no considerable differences between the plots.

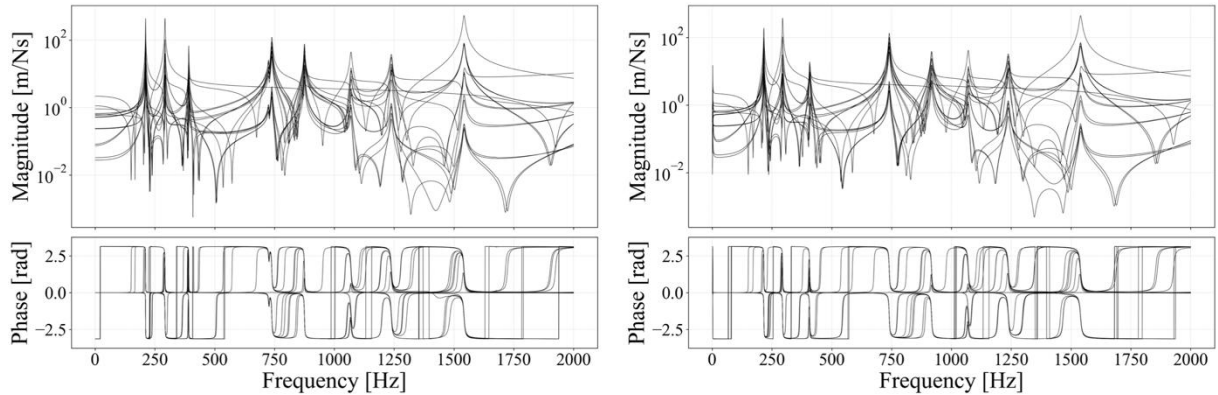


Figure 15: Overlaid FRFs of Experiment 1. Each line represents a specific force-response DoF combination of the assembled AM Structure. Left: LM-FBS coupling; right: reference.

3.2.3 Numerical FRF Comparison: LM-FBS Coupled vs. Reference

In this section, four pairs of numerical FRFs on the AM Structure are presented, each consisting of the LM-FBS coupled FRF and the corresponding reference FRF for a specific force-response DoF combination. Since there are four internal force and response DoFs specified (the DoF numbering follows the convention of Figure 12), a total of 16 force-response DoF combinations are available. The DoF placement allows for the generation of drive point FRFs, which indicate that both force and response DoFs are located at the same position of the structure [17][18]²⁰.

Below each displayed FRF, the coherence between LM-FBS and reference FRF is shown. It ranges from 0 (no agreement) to 1 (perfect agreement) and quantifies their similarity over the frequency range. The coherence is computed using the criterion presented in [19] (equations 19 and 20), originally proposed in [2], and captures differences in both amplitude and phase.

Figure 16 shows drive point FRFs for the assembled AM structure, one on the side of subsystem A (left plot) and one on the side of subsystem B (right plot). Aside from an approximate 40 Hz frequency shift near 900 Hz and a minor shift near 400 Hz, the respective curves show good visual agreement. High average coherence values of 0.988 and 0.951 support that. While only four resonance peaks are visible in the left plot of Figure 16, the right plot shows eight pronounced resonance peaks. The cause of this difference will be discussed in chapter 5.1.

²⁰ A distinction is made between true and approximate drive point FRFs, where true means force and response act on direct opposite sides of a solid structure, and approximate means they are separated by a gap or cavity [18]. That is, true drive points occur on subsystem A with no gap between force and response and approximate drive points occur on subsystem B with a gap between them (see e.g. force DoF 3 and response DoF 4 in Figure 12).

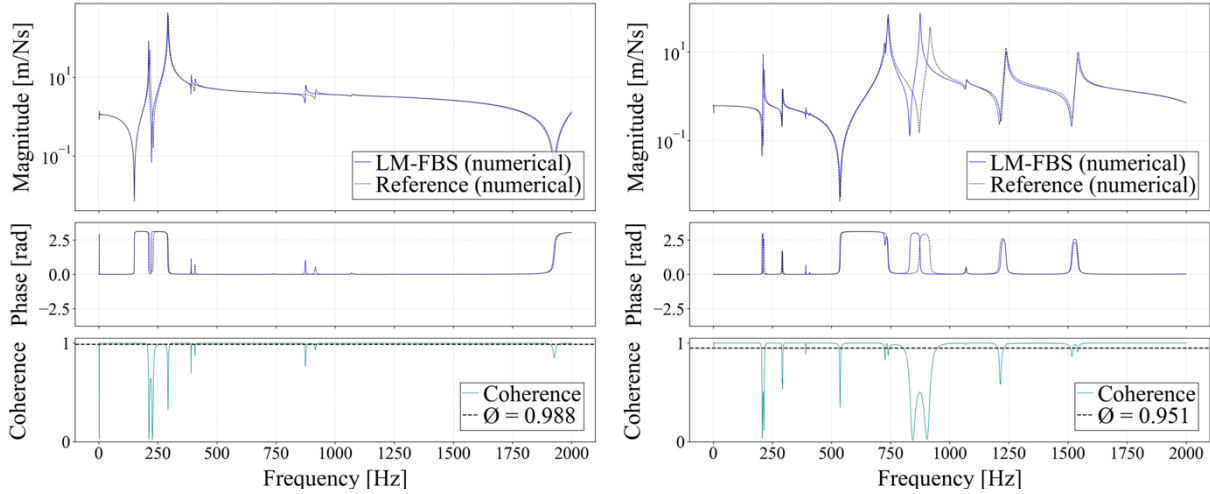


Figure 16: True (left) and approximate (right) drive point FRFs of Experiment 1.
Left: force DoF 1, response DoF 1. Right: force DoF 4, response DoF 3.

Figure 17 displays non-drive-point, internal FRFs (also referred to as cross FRFs in literature [20][21]). In the left figure, force and response are on opposite sides of the AM structure (force at subsystem A, response at subsystem B), whereas in the right figure, both force and response are within subsystem A. Similar to the driving point FRFs in Figure 16, the FRFs match closely besides an approximate 40 Hz frequency shift near 900 Hz, and a minor frequency shift near 400 Hz. With average coherence values of 0.938 and 0.954, the curves show good agreement, comparable to the FRFs in Figure 16. Although the left and the right plot of Figure 17 differ in shape, they show the same number of resonance peaks at comparable frequencies.

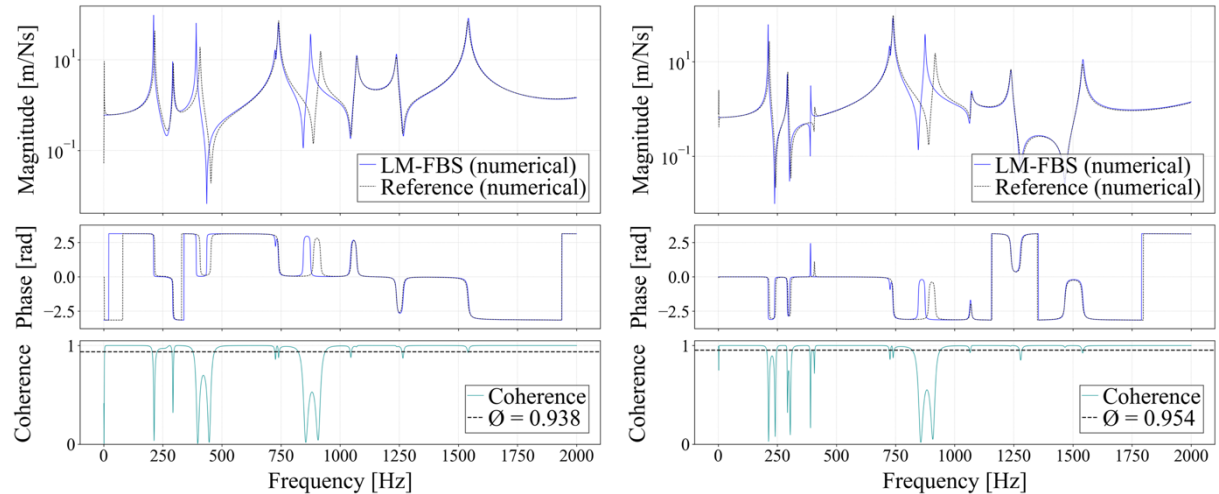


Figure 17: Examples of internal FRFs of Experiment 1.
Left: force DoF 2, response DoF 4. Right: force DoF 4, response DoF 4.

4 Experiment 2: Scanning Laser Doppler Vibrometry Experiment

Experiment 2 is the primary experiment of this thesis and the practical counterpart to Experiment 1, investigating the applicability of SLDV in FBS. It is carried out on the physical AM Structure using the same forces and responses (amount, placement, and orientation) as in Experiment 1, see section 3.1. Hence, there are 2 internal forces and responses, and 4 interface forces and responses per subsystem (A and B). Note that like in Experiment 1, the VPT is conducted in only one dimension (see 3.1 for clarification).

The excitation method in Experiment 2 is a piezoelectric actuator, corresponding to the 'forces' referred to thus far in this thesis, while the SLDV measurements represent the 'responses'. For the rest of this chapter, the 'forces' originating from the piezoelectric actuator will simply be referred to as excitations.

4.1 Experimental Framework

Figure 18 shows the disassembled AM Structure, made of aluminum, which exhibits light damping properties [16]. Both parts are machined from one aluminum block, which results in very similar mechanical properties: Young's modulus $E \approx 7.1 \times 10^{10}$ Pa; density $\rho \approx 2770 \text{ kg/m}^3$. Subsystems A and B have masses of approx. 1258 g and 1246 g, respectively.

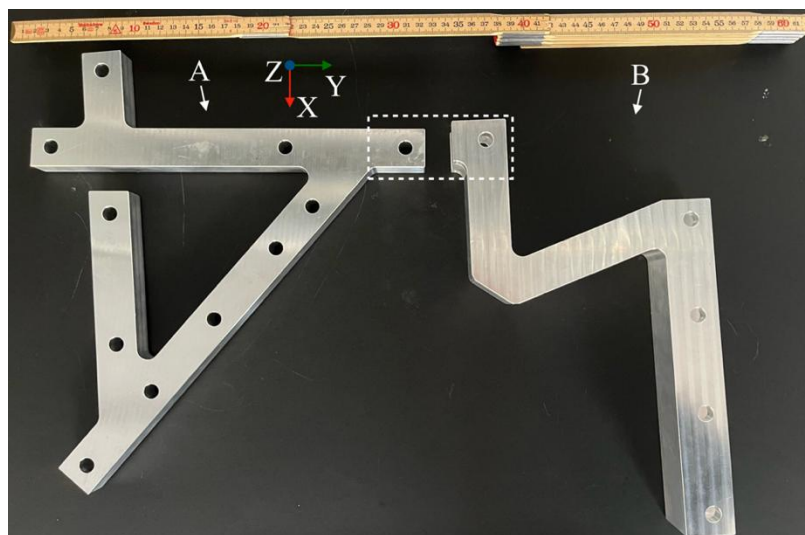


Figure 18: Disassembled AM structure comprising A and B. The interface region is highlighted by the white dashed rectangle.

For the reference measurements, A and B are connected using a hexagon socket head cap screw (M12, class 8.8), with top and bottom washers and a corresponding nut, tightened with a torque of 20 Nm (see Figure 19).

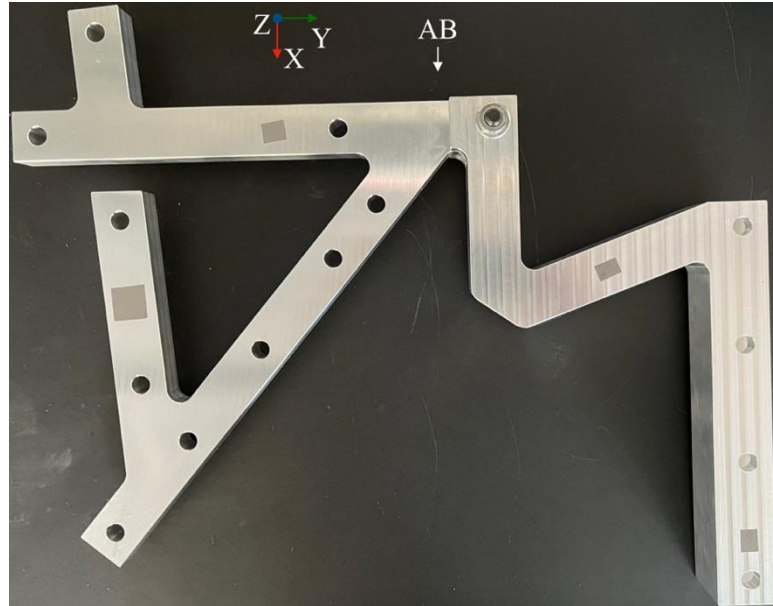


Figure 19: Assembled AM structure AB. The reflective tape (grey rectangles), placed at the response DoF locations, improves the signal-to-noise ratio of the SLDV.

Unlike Experiment 1, which yields numerical solutions for specified force-response DoF combinations instantaneously, Experiment 2 must be divided into several measurement campaigns: while the SLDV captures vibrations across all specified response DoFs in one measurement campaign, a separate campaign is needed for each excitation position. As there are 6 excitation DoFs (2 internal, 4 interface) for A and B, and 4 excitation DoFs (4 internal) for the reference AB, 16 measurement campaigns are to be made in total.

4.1.1 Technology of SLDV and its Application in Experimental Substructuring

Unlike conventional accelerometers, Laser Doppler Vibrometry (LDV) is a non-intrusive, highly precise measurement technique that uses a laser analyze the dynamic behavior of excited structures. In this way, measurements can be carried out without influencing the dynamics of the specimens. An additional benefit of utilizing a laser is that it does not have to be mounted, resulting in a high degree of repeatability. LDV exploits the Doppler effect that takes place when the laser gets reflected by the vibrating surface. Scanning Laser Doppler Vibrometry

(SLDV) expands upon LDV by automatically scanning over a predefined grid, allowing a high density of measurement points so that entire surfaces can be scanned over in one run. It enables the simultaneous²¹ acquisition of vibration responses across multiple degrees of freedom in a single scan – a clear advantage over LDV. Moreover, when paired with dedicated analysis software, SLDV enables a fast estimation of modal properties, such as mode shapes

In general, the Doppler effect can be noticed when there is a relative velocity between an observer and a wave-emitting source. In SLDV, this wave is the laser beam, and the vibrating object that reflects the beam acts as the wave-emitting source. The relative velocity occurs because the object is vibrating while the observer (the physical device) remains stationary.

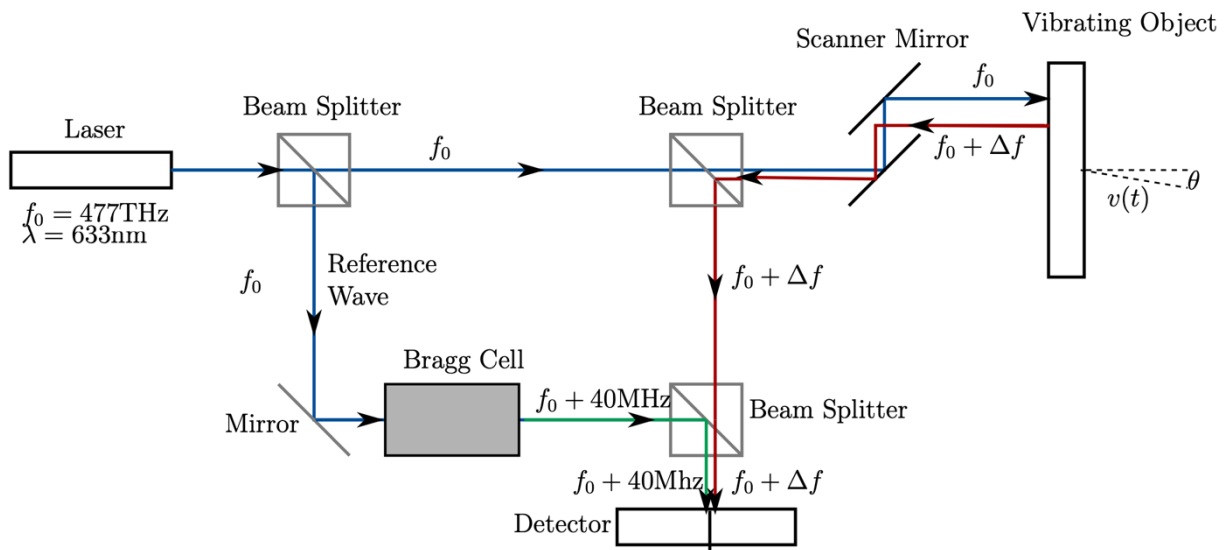


Figure 20: Schematic overview of the SLDV technology, taken from [22].

The precise working principle of the SLDV technology is illustrated in the schematic overview in Figure 20, taken from [22]. Here it can be seen that the Doppler shift is exploited by comparing a reference beam and a test beam. The test beam ($f_0 \approx 477$ THz) is directed at the vibrating object and reflected back. Due to the object's motion (with velocity $v(t) > 0$), it behaves like a moving wave-emitting source, causing a Doppler shift²² in the reflected beam's frequency. With a beam wavelength of 633nm, an angle θ of zero and a typical vibration velocity of 1m/s, the frequency shift is very small compared to f_0 . For this reason, the reference

²¹ ‘Simultaneous’ refers to a single automated scan run; the laser still measures each response DoF separately during that run.

²² The Doppler shift Δf can be calculated as $(2v/\lambda)\cos\theta$, where v is the velocity of the vibrating object, λ is the beam wavelength and θ is the angle between the beam and the object [22].

beam passes through a Bragg cell, which increases its frequency by 40MHz in order to be able to determine the sign of the Doppler shift Δf of the test beam. Eventually, the reference beam (shifted by 40 MHz) and the test beam (shifted by Δf) go through a photo detector, where the overall shift in frequency can be identified [22].

For the SLDV experiments in this paper, a PSV-500H vibrometer from Polytec Inc. is used. Specific properties of this device can be found in [23]. In Figure 21, the utilized SLDV equipment is shown.

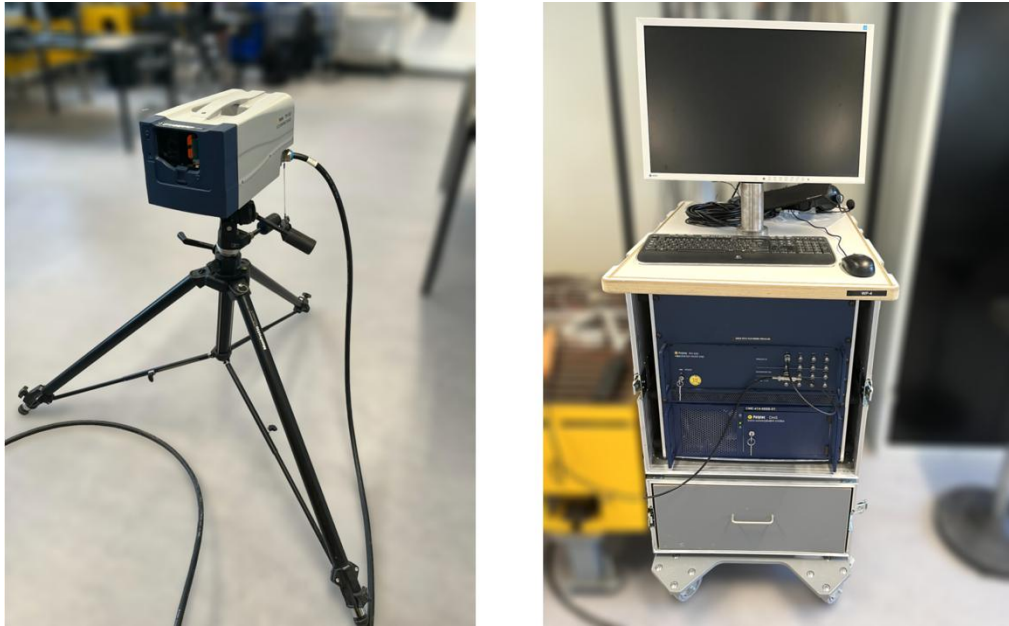


Figure 21: SLDV equipment at the Department of Civil and Mechanical Engineering (DTU) comprising a scanning head on a tripod (left) and a system rack (right)

4.1.2 Vibration Excitation Method

Although vibration experiments commonly use shakers or modal hammers as excitation sources, a piezoelectric actuator was selected in this study. A shaker was avoided because the experiment involves multiple excitation locations and rearranging the setup for each specific position would be impractical. Similarly, a modal hammer was evaded due to the large number of required hits – 16 excitation locations with multiple measurement positions each.

A piezoelectric actuator operates based on the inverse piezoelectric effect, where applying an electric voltage causes a piezoelectric material²³ to deform mechanically. This deformation produces precise movement, inducing forces that cause the attached structure to vibrate [24].

With the actuator, the AM Structure receives continuous excitation, which is necessary given that the SLDV response acquisition across multiple positions is not instantaneous. Moreover, a continuous excitation allows for a constant vibration pattern throughout measurements, ensuring the response is comparable across different excitation locations.

Figure 22 shows the piezoelectric actuator NAC2012-H6 from Noliac, which is used for Experiment 2. It is a multilayer actuator, consisting of multiple piezoelectric plates stacked on top of each other.

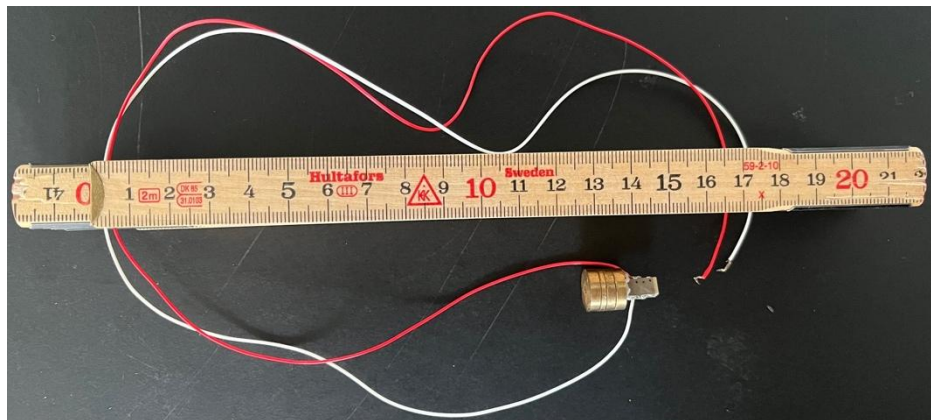


Figure 22: Piezoelectric actuator NAC2012-H6 from Noliac with brass reaction mass.

In Experiment 2, a brass reaction mass is glued to one side of the actuator to increase the maximum possible force the actuator can generate [25]. Note that the use of glue refers to superglue throughout this thesis. In addition, Figure 23 shows a steel, custom-made connector²⁴ glued to the other side of the actuator. Eventually, the assembly (comprising reaction mass, actuator, and connector) is glued to the AM Structure via the connector, as shown in Figure 23.

²³ Certain crystals exhibit piezoelectricity when their lattice lacks a center of symmetry, leading to surface charges under mechanical stress due to ionic polarization (dielectric materials). Most practical applications, however, use ferroelectric ceramics that produce greater strain and contain spontaneous electric dipoles [24].

²⁴ The connector is the head of a class 8.8 hexagon head bolt, with both sides filed flat to ensure full contact with the actuator and the AM structure, enabling effective vibration transfer.

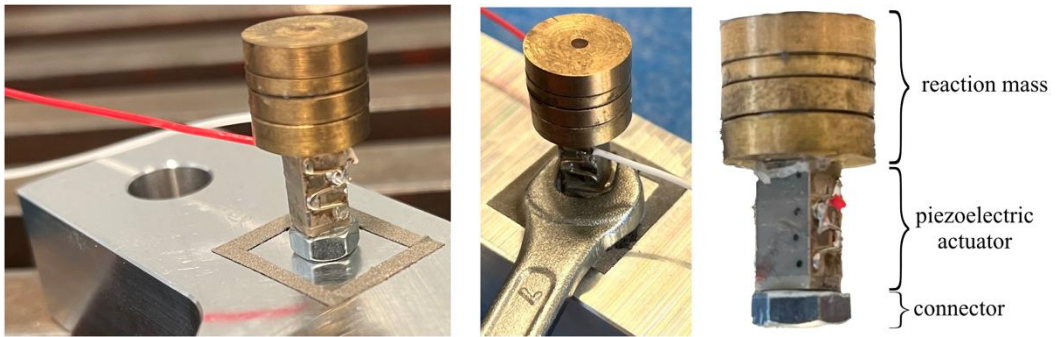


Figure 23: Piezoelectric actuator assembly comprising reaction mass, piezoelectric actuator, and connector. Left image: assembly glued to subsystem A. Middle image: detachment of assembly from subsystem A with a wrench (size 7).

The purpose of the connector is to facilitate the detachment of the assembly from the AM Structure. The use of superglue ensures a tight connection (good transfer of vibration) between the actuator and the AM Structure. Without the connector, the actuator would be glued to the AM Structure directly. This would pose a risk of damaging the actuator during 16 detachments (16 measurement campaigns), since the superglue's firm connection might be difficult to remove. Using the connector however, the detachment forces don't act on the actuator directly. Furthermore, the assembly can simply be detached using a wrench (see Figure 23), since the connector was made from a hexagon head bolt. The assembly's dynamic influence on the AM structure is negligible.

4.1.3 Experimental Setup

Figure 24 shows the physical setup, and Figure 25 illustrates how the components of Experiment 2 are logically connected in a block diagram. The AM structure (subsystem A in Figure 24) is suspended using rubber bands to approximate free-free boundary conditions.

The piezoelectric actuator assembly is glued to the desired excitation position and its cables are connected to the output of the power amplifier 2706 from B&K. The amplifier controls the power delivered to the piezoelectric actuator by amplifying a pseudo-random signal generated by the front-end of the system rack. The input of the power amplifier is connected to the output of the system rack's front-end. Additionally, a BNC-T connector is used to loop the front-end's output back to its input. The scanning head is connected to the system rack's back-end. The PSV acquisition software interacts with the system rack, enabling operation and monitoring of the experimental equipment. For an optimal signal-to-noise ratio, the distance from the laser beam exit point (in the scanning head) to the AM structure's surface should be approximately

an integer multiple of the laser's resonator length (20.4 cm for the PSV-500H's HeNe laser) [26]. This condition is met with a distance of 102 cm, equal to five times the 20.4 cm resonator length.



Figure 24: Experimental setup with blue labels showing relevant components. The system rack consists of the PSV-500 Front-End and the PSV-500 Back-End.

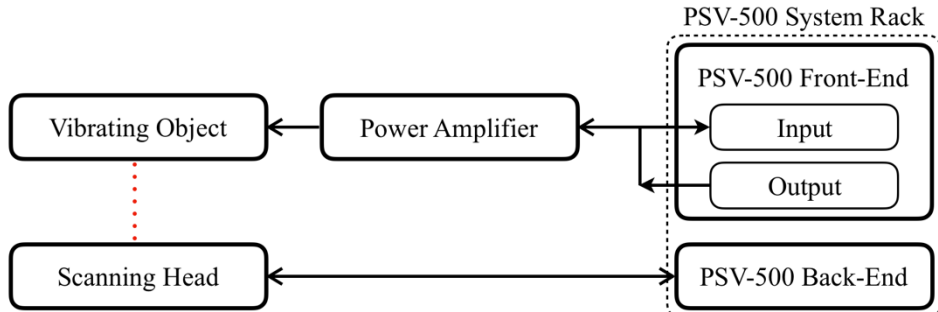


Figure 25: Block diagram of the experimental setup.

For the sake of completeness, the suspension setups for the other two configurations of the AM Structure (subsystem B and reference AB) are shown in Figure 26, with the rest of the experimental setup identical to that in Figure 24.



Figure 26: Suspension setup of subsystem B (left) and reference AB (right).

4.1.4 Flowchart of Experimental Data Generation and Processing

Experiment 2 involves multiple programs and several steps of data generation and processing. To avoid an extensive description, the flowchart presented in Figure 27 clarifies the workflow. The experimental preparation and execution (steps 1 and 2) are followed 16 times (\triangleq 16 sub-experiments), each corresponding to a distinct position of the piezoelectric actuator. The complete procedure for the SLDV and piezoelectric actuator equipment is shown in [26], covering steps 1 and 2 of Figure 27. The following paragraphs clarify specific steps in the flowchart, providing additional explanation where needed.

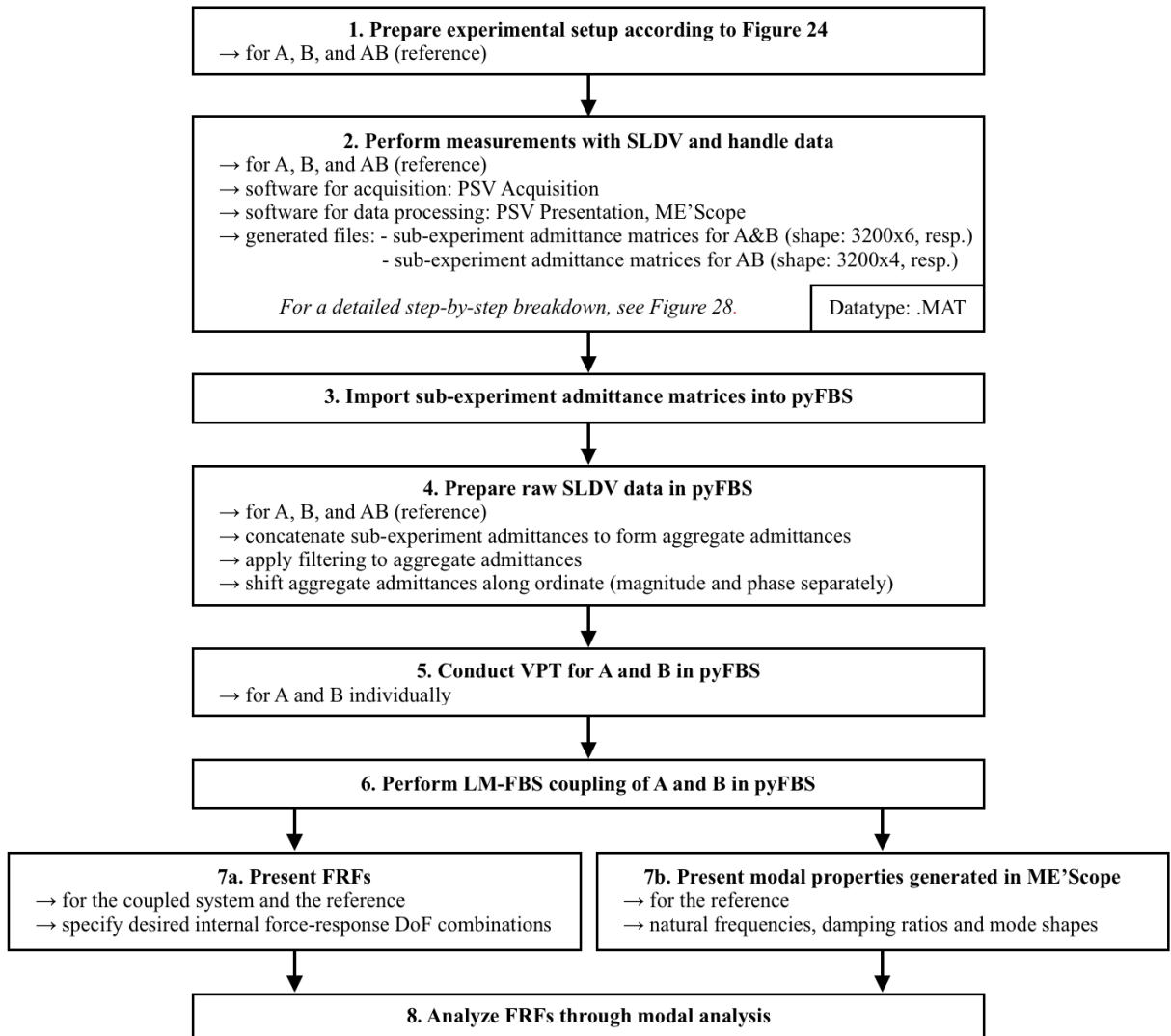


Figure 27: Flowchart of the SLDV experiment.

Once the experimental setup is prepared in step 1 according to Figure 24, SLDV measurements and data handling are carried out in step 2.

This step consists of a series of substeps, illustrated in the subprocess of Figure 28. Three different programs are utilized: PSV Acquisition and PSV Presentation (both from Polytec) are used for SLDV operation and initial result visualization, while ME'Scope is employed for more advanced modal analysis.

The unnumbered box 'Estimate modal properties for AB' has a dashed outline, as it is not part of the 16 sub-experiments (see beginning of this section). Instead, it is used in a dedicated

analysis²⁵ to extract the modal properties (natural frequencies, damping ratios and mode shapes) of the assembled AM Structure captured by the SLDV²⁶ in the specified frequency range. In contrast to the 16 sub-experiments, a full grid of laser measurement points was defined (in step 2.1) to provide enough data points for drawing meaningful conclusions about the mode shapes, see the comparison in Figure 29.

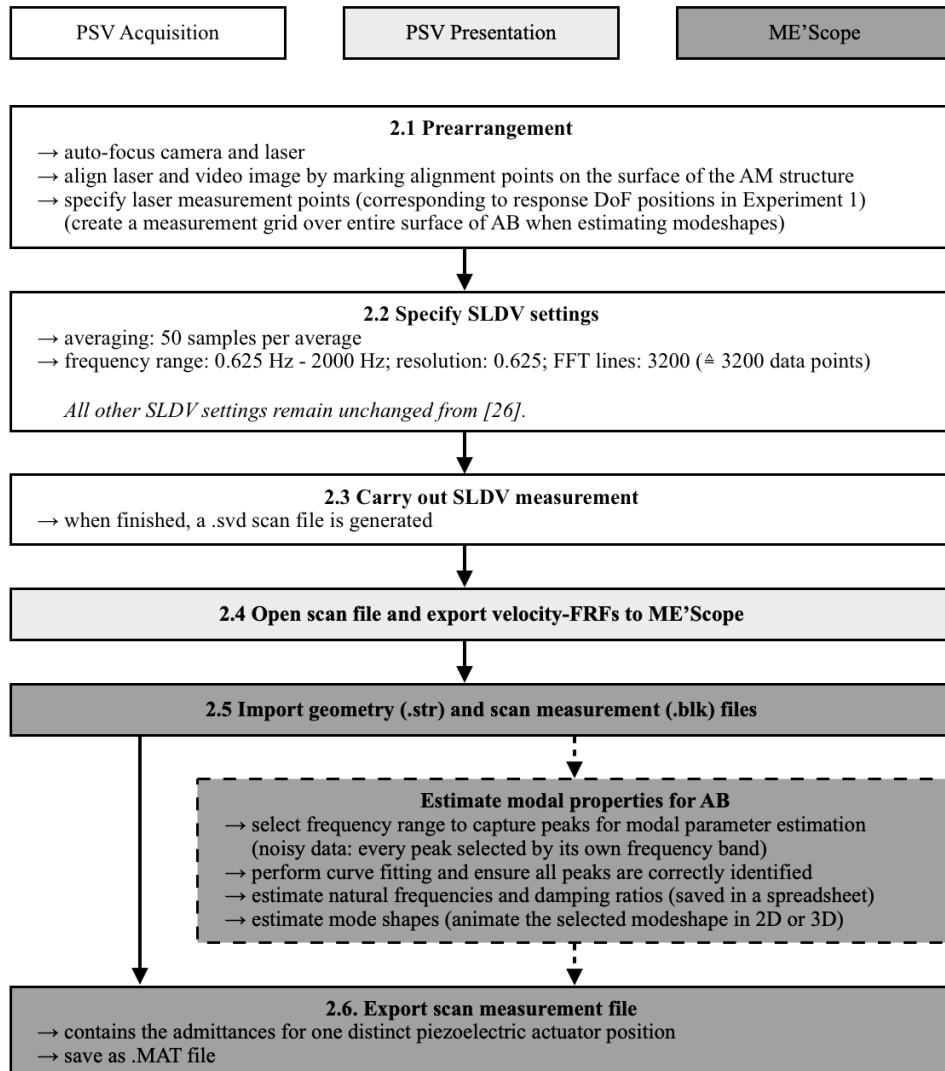


Figure 28: Subprocess of step 2 from Figure 27, covering the SLDV measurement and postprocessing steps of one sub-experiment. The colors of the steps correspond to the software used.

²⁵ For the dedicated analysis, excitation DoF 2 was used.

²⁶ The SLDV can only capture mode shapes that involve motion perpendicular to the measurement plane (Z-direction).

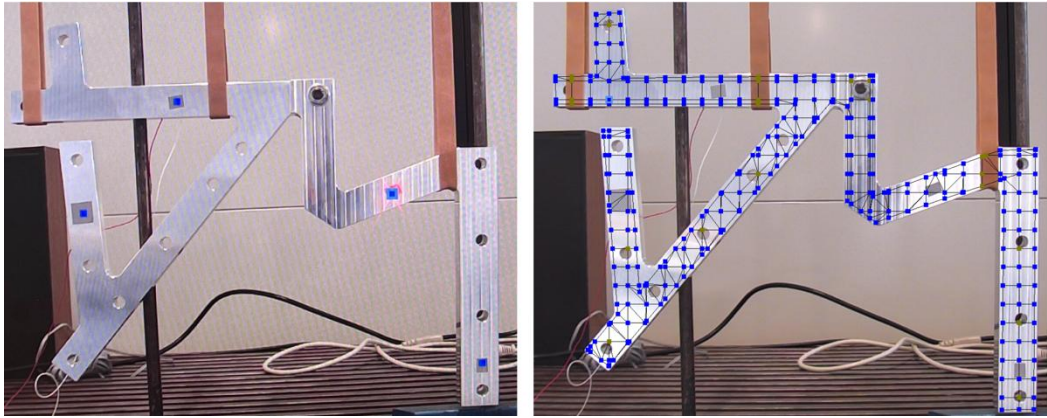


Figure 29: SLDV measurement point specification in PSV Acquisition. Blue and green squares mark activated and deactivated measurement points, respectively. The left image shows AB and its measurement points for one of the 16 sub-experiments (4 internal response DoFs). The right image shows a full measurement point grid, specifically created for the dedicated analysis aimed at estimating the modal parameters.

Each sub-experiment generates admittances for one force DoF (one distinct piezoelectric actuator position) and multiple response DoFs (number of laser measurement points). Once all admittances from the 16 sub-experiments are saved as .MAT files, they can be simultaneously imported into pyFBS in step 3.

Before performing the VPT with the pyFBS function *VPA.apply_VPT* (introduced in section 3.1.1; subsystem A used for demonstration) in step 5, the imported data, which still comprises raw SLDV data, must be prepared for the further process in step 4. Firstly, the sub-experiment admittances for A must be concatenated. Unlike in Experiment 1, where the admittances are obtained in a consolidated manner, in Experiment 2, the sub-experiment admittances are acquired individually for each sub-experiment, with each sub-experiment corresponding to a distinct excitation position. Since there are 6 excitation positions on A, this results in 6 sub-experiment admittances, each with a shape of $(6, 1, 3200)$ ²⁷. Recall that the admittance input array for *VPA.apply_VPT* (see section 3.1.1) includes all DoFs of A (all internal & interface excitations and all internal & interface responses), although only the interface DoFs are utilized for the VPT. Therefore, all 6 sub-experiment admittances of A are concatenated, converting

²⁷ For all 6 sub-experiments of A and B (comprising excitations at 2 internal and 4 interface DoFs), all 6 responses (4 interface and 2 internal) were measured, resulting in arrays of shape $(6, 1, 3200)$. Note that an additional array dimension has already been added.

them from 6 arrays of shape (6, 1, 3200) into a single array of shape (6, 6, 3200). The resulting aggregate admittance is then used as the admittance input for *VPA.apply_VPT* in step 5.

The aggregate admittances still contain noise from the SLDV measurements. This is primarily due to the piezoelectric actuator not applying a constant force across the frequency range. Its performance drops at low frequencies, leading to increased noise and reduced response levels. Furthermore, unlike a modal hammer, the piezoelectric actuator is a pure actuator and does not measure the applied force – the system rack’s front-end output is looped back to its input. As a result, the FRFs are not properly scaled and are merely amplified by an unknown factor from the power amplifier.

To mitigate the noise in the A and B measurement data, filtering is essential because the aggregate admittances are used in subsequent processing steps – such as VPT and LM-FBS coupling – where matrix inversions could amplify any unfiltered noise. For the reference AB, filtering primarily serves to reduce measurement noise without further downstream impact. The effect of the applied Wiener filter²⁸ is shown for subsystem B in Figure 30, where noise is visibly reduced. Figure 30 additionally illustrates the individual shifting of magnitude and phase along the ordinate to align with their numerical counterparts. Once the shifting and filter parameters are appropriately set in pyFBS, they remain consistent for all measurement data, since the excitation remains the same throughout.

After step 6 (LM-FBS), the coupled admittances again exhibit a fair amount of noise, as the VPT and LM-FBS matrix operations amplify residual noise remaining after the initial filtering in step 4. A secondary filtering step is therefore applied to the coupled data only. Note that the secondary filtering step is applied to a lesser extent than the first (first: Figure 30), and in general, filtering should be applied cautiously to avoid excessive distortion of the data.

In step 7b, the reference’s mode shapes, generated with ME’Scope, are presented. Since the SLDV captures vibrations exclusively along one dimension (Z-direction), the estimated mode shapes are limited to those exhibiting displacement in Z. This will further be elaborated in section 5.

²⁸ A Wiener filter is suitable for noise suppression, minimizing the mean square error between a desired signal and a noisy observation [33].

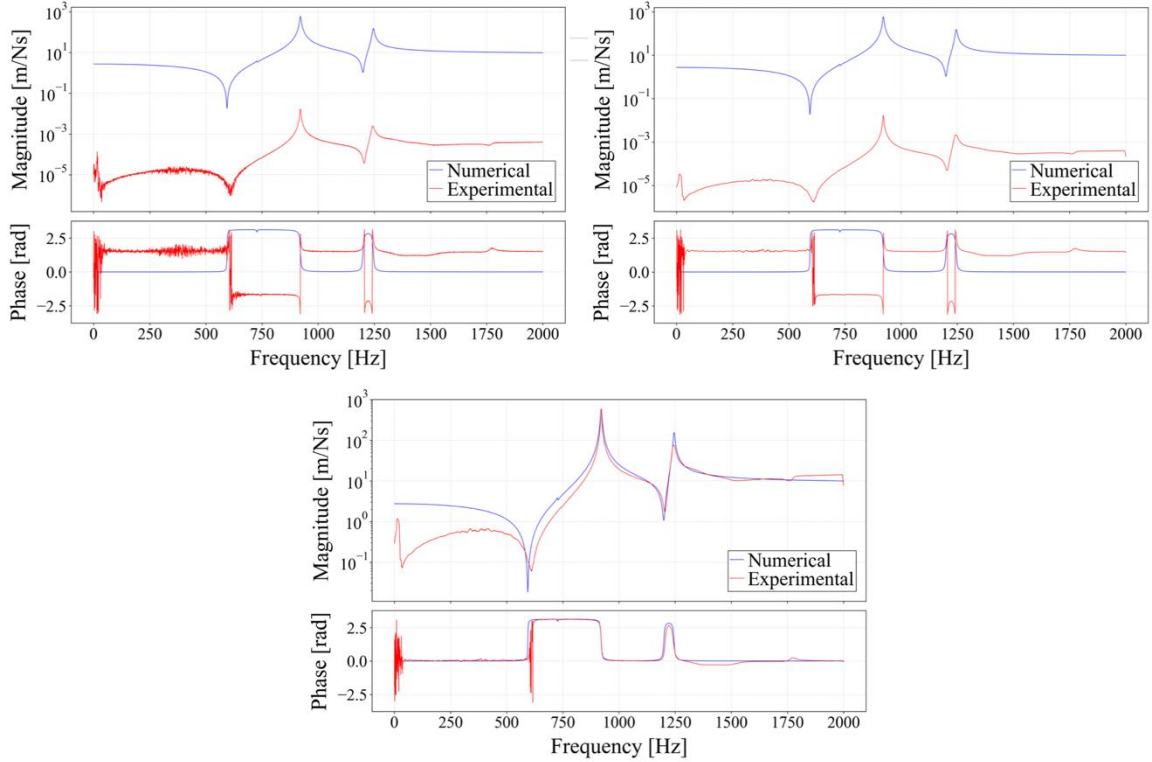


Figure 30: Numerical and experimental FRFs of subsystem B for example excitation and response DoFs. Raw experimental data (top left image) is filtered (top right image) and shifted (bottom image).

Steps 7a and 8 are carried out in accordance with their numerical counterparts, see section 3.1.1. To ensure an efficient plotting routine in pyFBS, the numbering of the DoFs in Experiment 1 and Experiment 2 was kept consistent.

4.2 Results of Experiment 2

This section presents the results of Experiment 2, following the same format as Experiment 1. Accordingly, the modal properties of the assembled AM Structure, including natural frequencies and mode shapes, are shown. Unlike Experiment 1, these properties are estimated using ME'Scope and additionally include damping ratios, since Experiment 2 is a physical experiment. Next, overlaid FRFs for all force-response combinations are presented, as well as a set of FRFs comparing the LM-FBS-coupled AM structure with the reference. Like in the numerical experiment, average coherence values are included for a quantitative comparison.

In addition to the coherence between the coupled and reference FRFs, we introduce another form of coherence – the measurement signal coherence – to evaluate the quality of the raw

SLDV measurement data. For each force-response combination, 50^{29} measurements are taken before averaging (see step 2.2 in Figure 28), and the coherence across these repeats can be plotted over the frequency range, including the corresponding average coherence value.

4.2.1 Measurement Signal Coherence

The first type of result presented is the measurement signal coherence, which indicates the quality of the acquired SLDV data. This type of coherence reflects the degree of linear correlation between the input (piezoelectric actuator) and output (SLDV measurements) evaluated across the frequency spectrum. High coherence values suggest reliable measurements and linearity, while drops in coherence may indicate noise, nonlinearity, or weak signal levels [26].

A large amount of data was accumulated throughout Experiment 2, which includes 16 sub-experiments corresponding to 16 different excitation positions: 6 positions each for A and B, and 4 positions for AB. Each sub-experiment for A and B uses 6 laser measurement points, while each for AB uses 4 – resulting in a total of 88 measurements. Each of these 88 measurements was sampled 50 times and averaged, resulting in 4400 individual samples.

Given the large number of potential coherence curves to display, only the coherences from the four AB sub-experiments are presented, with their force and response DoFs well distributed across the structure (see Figure 12).

Figure 31 shows the measurement signal coherences for each of the four AB sub-experiments across the frequency spectrum. For each sub-experiment, the coherence between the 50 samples at each of the four measurement points was first calculated, followed by averaging across the four points. The very low coherence values observed below 600 Hz, as well as additional characteristics of the figure are discussed in section 5.2.

²⁹ For a shaker, it is recommended to average across 32 to 64 measurements [34]. Since the piezoelectric actuator used in Experiment 2 is also a continuous excitation source, 50 measurements were taken before averaging.

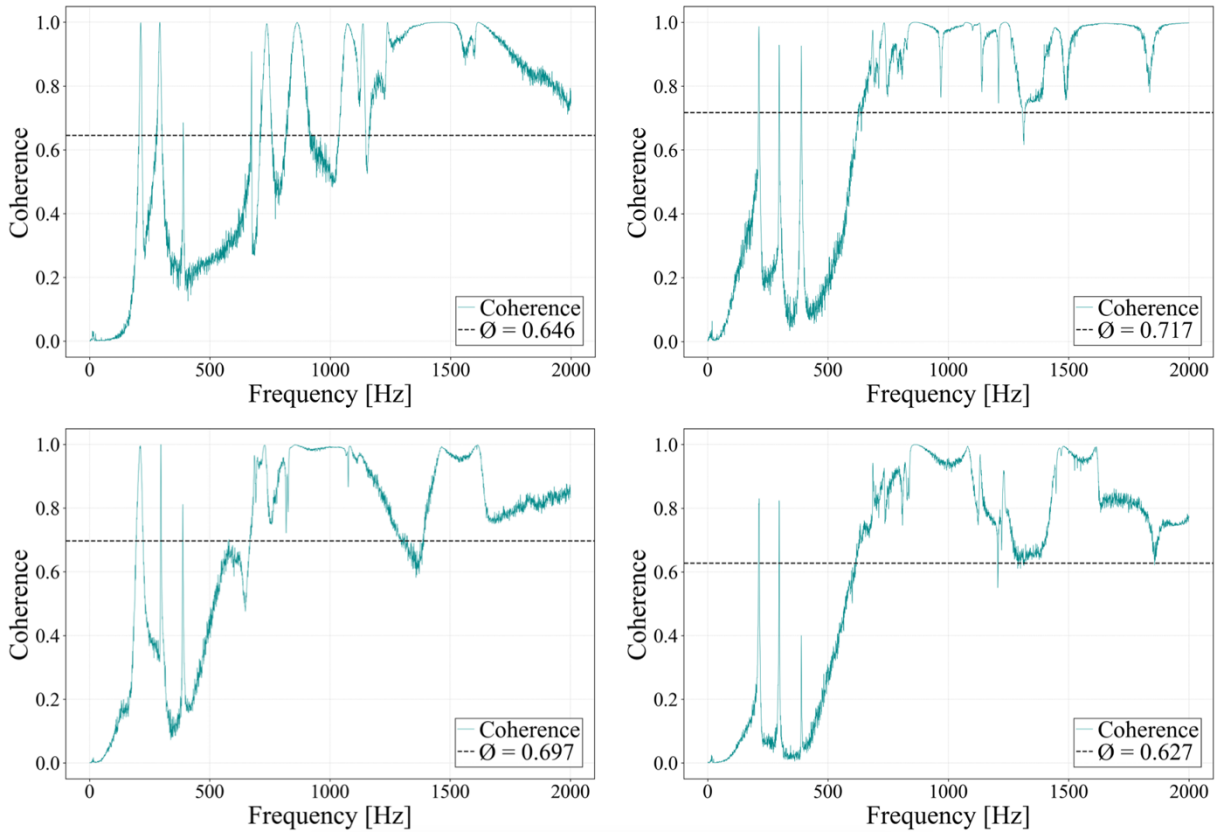


Figure 31: Measurement signal coherences of the four AB sub-experiments across the 0 to 2 kHz frequency spectrum, including average values. The top-left, top-right, bottom-left, and bottom-right plots correspond to force DoFs 1, 2, 3, and 4, respectively (see Figure 12 for DoF clarification).

4.2.2 Modal Properties: Natural Frequencies, Damping Ratios, and Mode Shapes

The modal properties of the reference AB are presented in this section. Natural frequencies, damping ratios and mode shapes are estimated using ME'Scope. The software is used to locate resonance peaks which correspond to the damped natural frequencies, and to perform advanced curve fitting for mode shape estimation (see section 4.1.4 or [26] for more details).

Note that since the SLDV only measures vibrations on the surface facing the device, the mode shapes simply represent the vibration behavior in the direction of the laser beam (Z-direction). Out-of-plane modeshapes cannot be captured with a 1D measurement campaign such as the one conducted in this thesis.

Figure 32 shows that within the 0 to 2 kHz frequency range, eight damped natural frequencies f_d^{30} , damping ratios ζ and mode shapes are identified. The majority of the damped natural frequencies lie in the lower frequency range, with only two out of eight located above 1.1 kHz. The damping ratios are in the range of 0.0121 to 0.439 %. The colors in the mode shape images represent vibration amplitude: green indicates low, blue moderate, and red high levels.

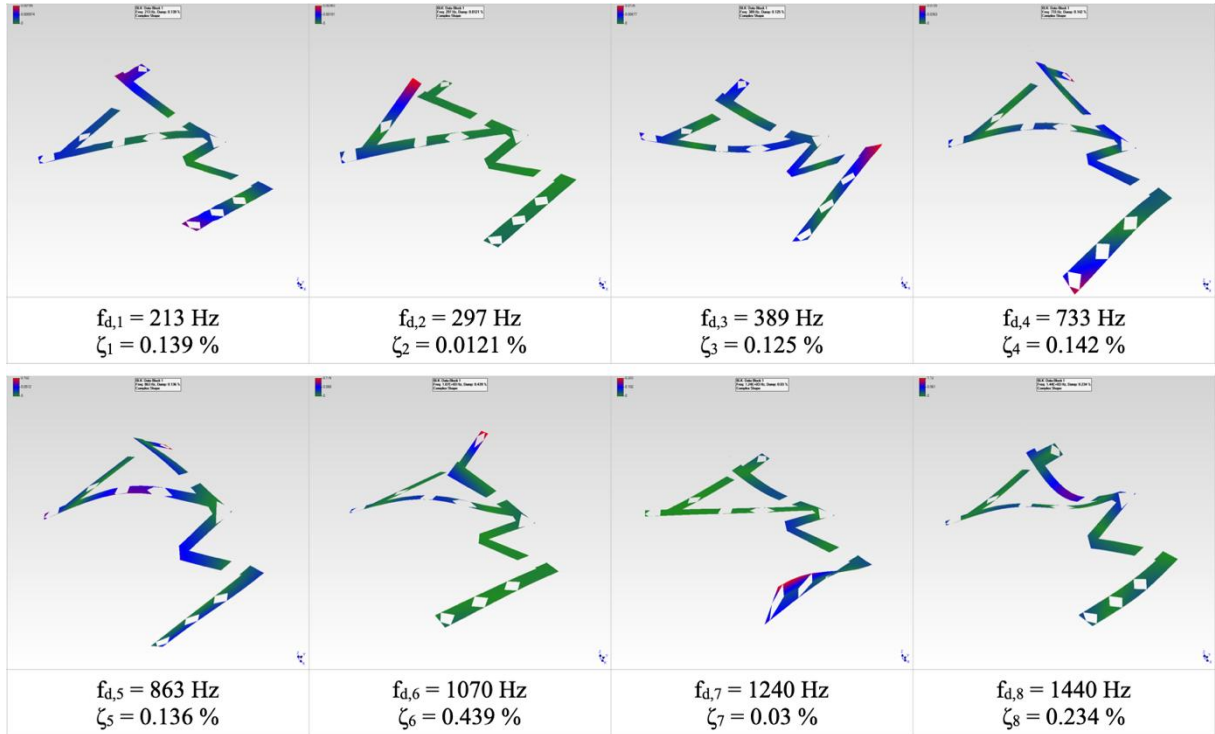


Figure 32: Experimentally estimated modal properties of AB, i.e. mode shapes, damped natural frequencies f_d and damping ratios ζ ; extracted from ME'Scope in the frequency range 0 to 2 kHz.

4.2.3 Overlaid Experimental FRFs of All Force-Response DoF Combinations

This subsection presents the overlaid FRFs for all 16 force-response combinations. Overlaid FRFs examine the presence of common resonance peaks across DoFs, helping to identify natural frequencies and mode shapes, and to visually assess the quality and consistency of the measurements.

³⁰ The natural frequencies discussed here are damped natural frequencies, as they are experimentally obtained from the physical system, which inherently includes damping.

Figure 33 shows the overlaid FRFs for the LM-FBS coupled AM structure (left plot) and the reference (right plot). Both plots exhibit increased noise at lower frequencies, but the reference plot has a lower overall noise level, making common resonance peaks easier to identify in the magnitude. However, due to the noise, the overlaid phase data is predominantly uninterpretable in both plots.

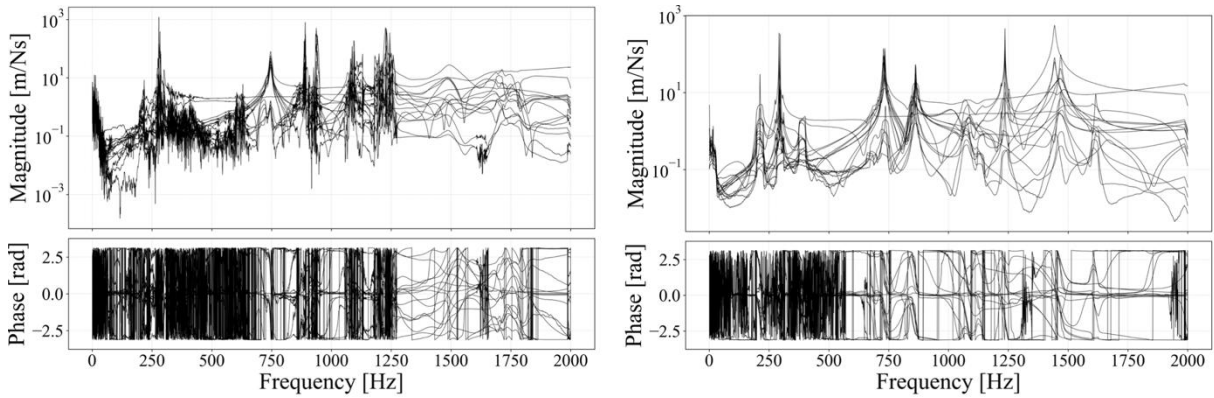


Figure 33: Overlaid FRFs of all force-response combinations of Experiment 2.
Left: LM-FBS coupling; right: reference.

4.2.4 Experimental FRF Comparison: LM-FBS coupled vs. Reference

In accordance with section 3.2.3, four pairs of FRFs from the AM Structure are presented: each pair consists of the experimental LM-FBS-coupled FRF and the corresponding reference FRF for a specific force-response DoF combination. Like in 3.2.3, the coherence shown below each FRF assesses the similarity between the LM-FBS-coupled and reference FRFs, using the same evaluation criterion.

Figure 34 shows drive point FRFs for the assembled AM Structure, one on the side of subsystem A (left plot), and one on the side of subsystem B (right plot). In both plots, the LM-FBS coupled curves exhibit more noise than the reference, especially at lower frequencies. Despite being based on experimental data, the curves demonstrate good agreement, with average coherence values of 0.932 and 0.850. This provides a first indication that an SLDV may be a suitable method for vibration measurement within the context of FBS.

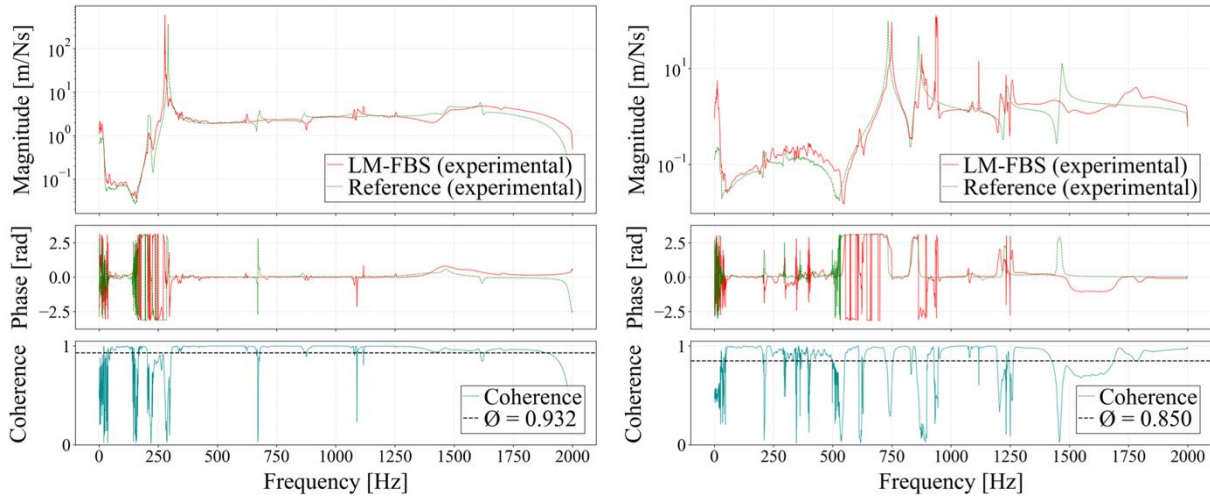


Figure 34: True (left) and approximate (right) drive point FRFs of Experiment 2.
Left: force DoF 1, response DoF 1. Right: force DoF 4, response DoF 3.

Figure 35 displays non-drive-point, internal FRFs (also referred to as cross FRFs [20][21]). In the left figure, the force and response are on opposite sides of the AM structure (force at subsystem A, response at subsystem B), whereas in the right figure, both are within subsystem A. Despite increased noise at low frequencies and the higher overall noise level of the LM-FBS coupled system compared to the reference, the curves show average coherence values of 0.738 and 0.827. In both plots, the coherence drops slightly at frequencies beyond 1250 Hz.

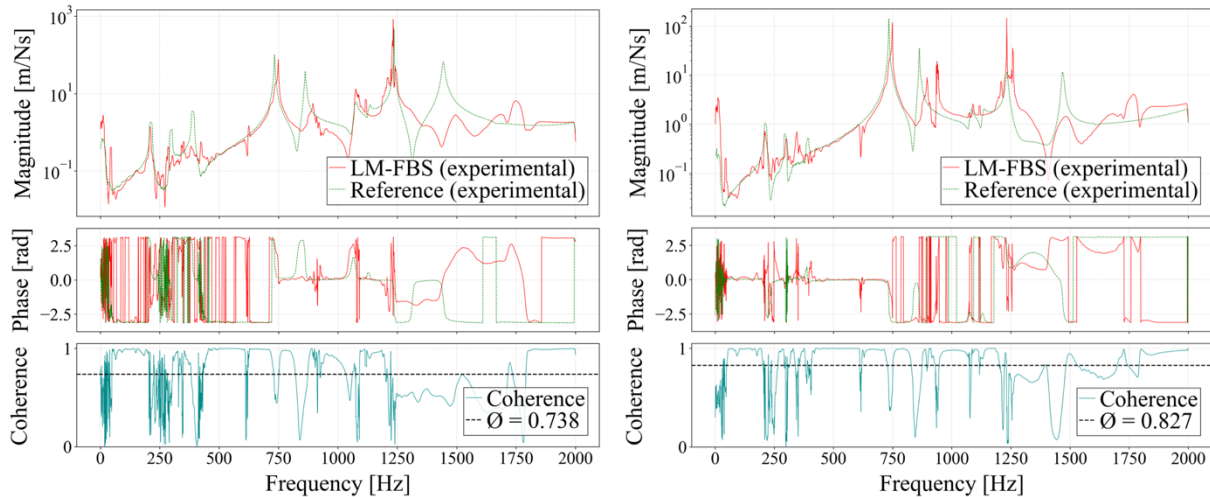


Figure 35: Examples of internal FRFs of Experiment 2.
Left: force DoF 2, response DoF 4. Right: force DoF 4, response DoF 4.

5 Discussion

This chapter discusses the results of the thesis. Since Experiments 1 and 2 were presented separately, they are also discussed in dedicated sections (5.1 and 5.2). Section 5.3 then compares the outcomes of both experiments. Lastly, section 5.4 directly evaluates the applicability of SLDV for FBS based on the experimental findings. As one of the main goals of the thesis, this section offers important insights into using SLDV in FBS, aimed at supporting future research in the field.

5.1 Discussion of Experiment 1 (Simulated Numerical Experiment)

The numerical analysis indicated 8 modeshapes on the assembled AM structure with distinguishable movement in the Z-direction in the frequency range 0 to 2 kHz. While the structure's cross section resembles a beam – rectangular on A and a mix of rectangular and U-shaped on B – its overall geometry is quite complex. As a result, many mode shapes become rather intricate and often cannot be described using simple deformation modes.

Nevertheless, some individual modes still exhibit beam-like deformation characteristics such as pure bending or torsion in certain sections (see Figure 14): bending occurs twice in mode 1 (both on A and B), and once in mode 2 (on A). Additionally, mode 7 displays significant torsion on B. Besides modes 2 and 7, mode 6 is one of the few where mainly one part of the structure moves while the other remains still. However, unlike modes 2 and 7, mode 6 involves a more complex combination of bending and torsion on A. The remaining mode shapes affect the entire AM Structure. Mode 3 primarily exhibits bending with a uniform curvature throughout, while modes 4 and 5 have a complex combination of bending and torsion.

An observation regarding frequency: as it increases, the mode shapes become increasingly complex in their deformation patterns. For instance, in mode 1, part A experiences simple bending with maximum deflection at the end, while in mode 8, the same region shows peak deformation near the center, creating a bending node close to the branch at the arm's end. This trend continues in higher modes (not shown), where rising frequency leads to more intricate vibration patterns and multiple bending and torsional nodes along the structure's arms.

The presence of eight resonance frequencies – each exciting modes with motion in the Z direction – can also be identified in Figure 15, which displays the overlaid FRFs for all available force-response DoF combinations (LM-FBS coupled vs. reference). Since natural frequencies

are inherent structure properties, the resonance peaks in the reference magnitude of Figure 15 appear at these natural frequencies (shown in Figure 14), regardless of the specific force-response combination³¹. What varies between combinations is not the frequency of the peaks, but their amplitude, which depends on how strongly each mode is excited and observed at the respective DoF.

Unlike the magnitudes, several phase curves do exhibit a variation in frequency in the reference plot of Figure 15. Before explaining this difference, some background on resonances and antiresonances is necessary. Antiresonances appear as dips or minima in the magnitude and correspond to the zeros of the FRF [27], arising from destructive interference between vibration modes [17]. In contrast to resonances, antiresonances are not inherent structural properties [27]; their frequency locations can vary with the selected force-response combination [28]. At antiresonances, the phase typically undergoes a shift of π , while at resonances it shifts by approximately $-\pi$ [27] [29]³².

Returning to the question of why the overlaid phase plots differ in frequency across force-response combinations: the difference cannot be linked to the occurrence of resonances in the magnitudes, since their (natural) frequencies are the same across all combinations. The variation must therefore be linked to the antiresonances, with two main factors being responsible. First, the number of antiresonances can vary between FRFs depending on the specific force-response pairing [27]: some FRFs may exhibit an antiresonance (and thus a phase shift of π) near a certain (antiresonance) frequency, while others do not. Such a variation means that the phases of some combinations will shift at a certain frequency, while the phases of other combinations won't. Second, even if an antiresonance is present near a such an (antiresonance) frequency, the exact frequency of it may differ between FRFs, as antiresonances are not invariant structural properties [28]. In turn, variations in (antiresonance) frequencies in the magnitude result in variations of where the phase shift of π takes place between different phase curves.

With the overlaid reference plot of Figure 15 now discussed, we proceed to the comparison between the reference and LM-FBS simulations. The overlaid reference and LM-FBS FRFs reveal no significant visual difference. However, for a more meaningful comparison, the FRFs

³¹ With small damping, the difference between damped (resonance) frequencies and undamped natural frequencies is insignificant [26] (damping ratio $\zeta = 0.3\%$ assumed for FRF synthetization in pyFBS).

³² The extent of these phase shifts may vary in figures due to the influence of damping and specified frequency resolution.

of individual force-response combinations (such as those in Figure 16 and Figure 17) should be compared directly.

First, some general observations from Figure 16 and Figure 17: The previously discussed phase shifts of $\pm\pi$ at resonances and antiresonances are clearly visible in all plots, with the transitions smoothed due to the light damping introduced during the FRF synthetization. A characteristic feature of driving-point FRFs is that each antiresonance occurs between a pair of resonances [27]. This pattern is evident in Figure 16 (driving-point FRFs), but not consistently in Figure 17 (non-driving-point FRFs), where multiple resonances or antiresonances appear consecutively without the alteration observed for driving-points.

Three out of the four plots in Figure 16 and Figure 17 display all eight resonance peaks, corresponding to the eight mode shapes presented in Figure 14. However, the first driving-point FRF shown (the left plot in Figure 16) exhibits only four visible resonance peaks, indicating a potential outlier. This suspicion is confirmed upon revisiting the overlaid FRFs in Figure 15: while most curves clearly show all eight resonance peaks, the first driving-point FRF stands out as it remains nearly horizontal across most of the frequency range. The reason behind this can be explained by looking at the position of the driving point (force DoF 1, response DoF 1; see DoF naming in Figure 12) throughout the mode shapes in Figure 14: At 216 (turquoise; 1st mode) and 294 Hz (green, 2nd mode), the colors indicate rather high vibration amplitudes. At 408 (light blue; 3rd mode) and 918 Hz (light blue, 5th mode), the colors indicate moderate to low vibration amplitudes. These observations are reflected in the FRF magnitude of Figure 16 (left plot), which displays two larger and two smaller resonance peaks. However, for all other modes (4, 6, 7, and 8), the driving point remains in the dark blue color range, indicating very low vibration amplitudes. Low vibration amplitudes correspond to low response levels; and since an FRF is the ratio of response to force, no resonance peaks are visible for these modes.

Figure 16 and Figure 17 demonstrate a strong visual agreement between LM-FBS coupled and corresponding reference curves, indicating successful coupling. This is supported by the high average coherence values, which are all above 0.9. However, noticeable discrepancies appear at two specific frequency regions, where mismatches are observed in both frequency and amplitude. Since these discrepancies consistently occur across all four plots, they appear to be independent of the specific force-response DoF combinations. This points to the coupling as a possible cause of the differences.

The first, main discrepancy occurs near 900 Hz, exhibiting an approximate 40 Hz frequency shift. The observed shift is likely linked to the VPT, whose validity may be compromised when the interface experiences high loading. Such high loading at the interface occurs at 918 Hz, as deduced from the 5th mode shape shown in Figure 14: although the interface region itself does not vibrate significantly (indicated by the dark blue color), it is precisely this region that accommodates the opposing nature of movement of A and B.

At the 5th mode shape's snapshot in Figure 14, the two arms of A (near the interface) and the arm of B (near the interface) have inertia in opposite Z-directions. Unlike other modes, where the regions on either side of the interface often move in an aligned manner, mode 5 is different. Parts A and B exhibit movement along opposing paths and the interface region acts as the separation boundary between these conflicting motion paths. This results in heavy loading of the interface, which is the presumable cause of the frequency shift around 900 Hz. Two underlying effects can explain the shift: First, the heavy interface loading causes increased local deformation at the interface, likely invalidating the VPT rigidity assumption near this frequency. Second, the complex torsion and bending in the 5th mode may cause shifts in X and Y and rotation about Z that the 1D VPT cannot capture.

The second, minor discrepancy in the plots of Figure 16 and Figure 17 occurs near 400 Hz. This frequency is associated with the 3rd mode, which primarily shows bending with a uniform curvature throughout the structure. In bending, one side of the neutral plane undergoes compression while the opposite side experiences elongation. At the interface, this can introduce flexibility since the adjacent regions of parts A and B are not constrained in the X and Y translational directions. As a result, slight relative movement may occur at the interface, potentially contributing to the observed discrepancy.

5.2 Discussion of Experiment 2 (SLDV Experiment)

It is obvious that conditions in physical laboratory experiments are less controlled than in numerical simulations. Quantifying the impact of this variability is essential for a scientific evaluation of the final results. This was done using the measurement signal coherence shown in Figure 31, which provides a measure of how consistent and repeatable the SLDV measurements are when testing the same sample in the same position³³.

At first glance, the plots show a lot of inconsistency in the coherence curves. Overall, all the plots display very low coherence below 600 Hz, followed by a sharp increase at around 600 Hz, where coherence remains high up to 2000 Hz. Interestingly, below 600 Hz, the coherence spikes three times – corresponding to the first three resonance frequencies. This behavior suggests that at these resonance points, the system response is strong and linear enough to produce clear, repeatable measurements, resulting in high coherence. Such a pattern is in contrast with common observations where coherence often drops at resonances due to nonlinear effects, noise, or modal coupling [26]. Additionally, coherence may decrease at antiresonances because the response is very low, causing the sensor to pick up mostly noise [26] – the drops in coherence at higher frequencies are therefore likely linked to resonances and antiresonances. While the coherence curves vary visually and quantitatively (ϕ values 0.627 - 0.717) across the four plots in Figure 31, meaningful interpretation of these differences is limited, as each plot shows averaged coherence over all response DoFs for each excitation DoF.

Overall, Figure 31 shows low measurement repeatability below 600 Hz, along with the presence of noise throughout the signal – likely related to the limited performance of the piezoelectric actuator. At lower frequencies, the actuator fails to excite with the same magnitude as at higher frequencies (a constant excitation magnitude is intended, as the power amplification stays constant). Since the actuator lacks a load cell (unlike a modal hammer), this magnitude discrepancy cannot be compensated for. Consequently, because coherence is low below 600 Hz, the FRFs in that range are not reliable.

Figure 32 shows eight experimentally estimated mode shapes within the 0 to 2 kHz frequency range. While they appear flat (the SLDV measures only the surface layer), they exhibit the same

³³ Note that the plots of Figure 31 represent averaged coherences; see section **Error! Reference source not found.** for clarification.

vibration patterns as the numerical mode shapes presented in section 3.2.1³⁴. Each mode shape corresponds to an estimated damped natural frequency and damping ratio. The damping ratios range from 0.0121 % to 0.439 %, confirming the initial assumption of very low damping in aluminum. Regarding the variation in the damping ratios: a higher ratio means vibration in that mode decays faster with broader FRF peaks; a lower ratio means it lasts longer and the peaks appear sharper.

Such a characteristic is evident in the overlaid FRF reference plot of Figure 33, where the 6th resonance frequency – which corresponds to by far the highest damping ratio in Figure 32 (0.439 %) – displays noticeably rounder resonance peaks compared to the other modes.

Another observation regarding the overlaid reference FRFs is that (unlike the estimated modal properties), some experimental curves exhibit an additional 9th resonance peak near 1650 Hz. This extra peak appears mainly for force-response combinations involving DoF 1, which is located near a free end of subsystem A. One possible explanation is that the bolt connection introduces interface flexibility (i.e., it is not perfectly rigid), leading to mode localization, where deformation is concentrated in a small region of the structure [30]. For modal properties estimation, a dedicated test run (see section 4.1.4) was conducted with excitation applied only at DoF 2. Because DoF 1 was not excited, the localized mode there may have gone undetected by ME'Scope, resulting in only eight identified mode shapes.

The overlaid LM-FBS plot of Figure 33 shows significantly more noise than the reference, especially for frequencies below 600 Hz. This is expected, as Figure 31 shows poor force-response correlation below 600 Hz³⁵. In general, while multiple common resonance peaks are present, not all of them are clearly visible and distinguishable when they are overlaid. The observation is likely linked to noise amplification during the VPT and LM-FBS, as the matrix inversions involved tend to amplify noise introduced by the piezoelectric actuator. Additionally, inherent noise in the measurements contributes to this effect.

Compared to the reference, the curves above 1250 Hz appear considerably damped and inconsistent – likely caused by noise effects and the VPT (limited DoF coupling; unfulfilled rigidity assumption). For a more meaningful comparison of the coupled and reference FRF

³⁴ For a detailed analysis of the vibration patterns, refer to the numerical discussion in section 5.1.

³⁵ Although Figure 31 only presents coherence for AB (not for A and B separately), it reveals a clear trend of low measurement repeatability at low frequencies.

results, individual DoF combinations (such as those in Figure 34 and Figure 35) should be directly compared.

Figure 34 and Figure 35 demonstrate sound agreement between the LM-FBS coupled and corresponding reference curves, supported by average coherence values ranging from 0.738 to 0.932. In all plots, the reference exhibits less noise than the coupled FRF, which shows numerous smaller (and some larger) spikes between the actual resonance peaks, causing the coherence to drop at those frequencies. Revisiting the observation from the previous paragraph, coupled FRFs above 1250 Hz appear significantly damped and inconsistent. In contrast, the reference FRFs show a single, well-defined peak around 1440 Hz³⁶, causing a drop in coherence above 1250 Hz in the respective plots. Two reasons might contribute to this deviation, the first one being the influence of the localized 9th mode around 1650 Hz for some DoF combinations (see discussion of Figure 33). Secondly, in the mode shape at 1440 Hz, the structure's interface experiences large vibration amplitudes. This may influence the accuracy of the one-dimensional VPT, which allows relative displacements in X and Y and rotations around Z.

Near 900 Hz, the LM-FBS curves in the overlaid FRF plot exhibit two closely spaced peaks instead of a single resonance peak. Figure 34 and Figure 35 further reveal a frequency shift between the LM-FBS and reference curves in this region. This behavior occurs near the 5th mode, which has a complex vibration pattern, with the two arms of A and the arm of B having inertia in opposite Z-directions near the interface (see Figure 32). The interface region forms the boundary between these opposing motions, resulting in significant interface loading, which may explain the irregularities observed near 900 Hz. As this behavior was also observed in Experiment 1, a detailed analysis is provided in 5.1.

³⁶ Not relevant for the DoF 1 driving-point FRF outlier (left plot in Figure 34; see section 5.1 for discussion).

5.3 Experiment 1 vs. Experiment 2

The findings from Experiments 1 and 2 are compared in this section. Although the goal of the thesis is not to perfectly match the numerical and experimental results, a comparison helps to identify experimental limitations and validate the numerical model.

Starting with the modal properties, the mode shapes in Figure 14 and Figure 32 show consistent vibration patterns across the frequency range, indicating that the rubber band suspension in Experiment 2 successfully approximated free-free boundary conditions. The natural frequencies indicate good overall agreement as well: except for the third, fifth, and eighth natural frequencies (showing differences of 19, 55 and 101 Hz, respectively), all other frequencies differ by less than 7 Hz. Although Figure 14 shows undamped and Figure 32 shows damped natural frequencies, good agreement is expected due to the low damping in Experiment 2³⁷. The discrepancies in the third, fifth, and eighth modes are likely linked to the interface connection. In Experiment 2, the reference consists of two parts connected by a physical bolt (introducing added mass and flexibility), whereas in Experiment 1 it is modeled as a single part. Since the mentioned modes involve increased vibration or loading at the interface, the difference in connection likely contributes to the observed deviations.

Figure 36 presents the overlaid FRFs of Experiments 1 and 2 for one selected DoF combination (force DoF 1 and response DoF 4), serving as a representative example of the effects discussed. Overall, the resonance peaks are visible for most of the curves, with their peaks agreeing in frequency. Below 600 Hz, the curves from Experiment 2 show a noticeable decrease in magnitude compared to those from Experiment 1. This difference is expected, as poor measurement signal coherences (shown in Figure 31) in this frequency range were already observed and discussed in section 5.2. Nevertheless, the resonance peaks of the curves below 600 Hz are largely aligned in frequency.

For modes 4, 6 and 7, the natural frequencies agree well, although the magnitudes of Experiment 2 are much higher for mode 7. A possible explanation for the difference is that mode 7 has a very low damping ratio ($\zeta_7 = 0.03 \%$), while the numerical model assumes a uniform damping of 0.3 %. Since higher damping tends to round resonance peaks, this difference in damping may contribute to the observed discrepancy. Regarding mode 5, a

³⁷ Note the classical relationship between damped (f_d) and undamped (f_n) natural frequencies: $f_d = f_n (1 - \zeta^2)^{0.5}$.

variation in natural frequency can be observed between the FRFs. As discussed in sections 5.1 and 5.2, this variation is linked to heavy interface loading caused by the distinct vibration pattern of mode 5.

Although the shape of the 8th resonance peak is similar between Experiment 1 and the reference of Experiment 2, there is a significant frequency shift. This is likely because the reference in Experiment 2 is connected with a physical bolt assembly, which adds mass and introduces residual interface flexibility (unlike the reference in Experiment 1). Since the interface experiences high vibration amplitudes in the 8th mode, this effect becomes significant. For further information regarding this characteristic, refer to section 5.2, where it is discussed in detail.

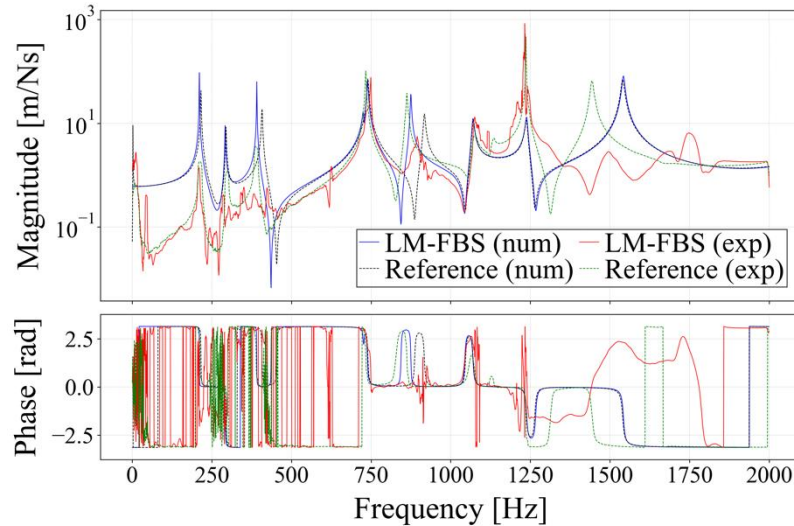


Figure 36: Overlaid FRFs of Experiment 1 (num) and Experiment 2 (exp) for force DoF 2 and response DoF 4.

5.4 Applicability of SLDV in FBS

The experiments conducted in this thesis successfully demonstrated the feasibility of using SLDV for response measurement in FBS. Its advantages over conventional techniques – particularly in the FBS context – will be detailed in section 5.4.1.

The study also encountered several challenges, both due to the SLDV's fundamentally different characteristics compared to traditional accelerometers and the influence of the excitation method (since FRFs inherently depend on both response and excitation). In Experiment 2, for example, the use of a piezoelectric actuator – while providing certain advantages – contributed to the low measurement signal coherence, especially at lower frequencies, and thereby affected the quality of the final results. These and other experimental limitations are discussed in detail in section 5.4.2.

5.4.1 Strengths of the Experimental Framework for Experiment 2

One big advantage of the Experiment 2 framework is that it allows for measuring many response DoFs at once within a single SLDV scan. In practice, this means that an arbitrary number of points on the structure's surface facing the SLDV can be recorded for every excitation position. These points can then serve as internal or interface response DoFs.

Without the SLDV's scanning feature, gathering FRFs for 16 different force-response combinations would have taken significantly longer. As the SLDV moved from one response DoF to another, it averaged 50 samples for each DoF combination – equivalent to 50 separate modal hammer impacts (+ accelerometer measurements) for just that single response point. The main time-consuming step was re-mounting the piezoelectric actuator between tests. Once the actuator was in place, the rest of the experimental execution (steps 1 and 2 in Figure 27) proceeded quickly since the actuator provided continuous excitation throughout each scan. Another benefit of the actuator was its small size, allowing for quick repositioning between tests. In contrast, larger continuous excitation methods like shakers are bulkier and more difficult to move.

Since the VPT requires multiple response DoFs in proximity to the coupling interface, space constraints may become an issue with conventional sensors such as accelerometers. No such limitations are encountered with the SLDV equipment since the PSV Acquisition software allows for setting a dense grid of scan points. Note that an even denser interface grid was tested

in the numerical study (16 interface responses instead of 4), but it was discarded as it yielded virtually the same numerical coupling results as the configuration with 4 interface responses. This is mentioned to clarify that such a denser setup would have also been easily possible with the SLDV. In fact, a fairly dense grid (see Figure 29 – which could be made even denser) was used to estimate modal properties with ME'Scope. This allowed for a clear and detailed 2D visualization of the mode shapes. Such fast and detailed mode shape estimation in two dimensions (along with clear visualization) is difficult to achieve with conventional tools and further demonstrates the practical strengths of the SLDV system.

Another benefit of using the SLDV equipment is its straightforward operation – provided that good user instructions are available (such as in [26]), the SLDV and its softwares are easy to use. When paired with a piezoelectric actuator, common vibration testing issues like “double hits”, which can occur when using a modal hammer for excitation, are completely avoided. Overall, the SLDV system offers a user-friendly and reliable setup.

The 1D VPT performed better than expected with the chosen AM structure. Not coupling all DoFs did not significantly affect the FRFs along the Z-axis, however, this may not be generally valid. In this particular case, the geometry of the AM structure, combined with the specific choice of which DoFs were coupled and which were not, happened to be well-suited.

5.4.2 Limitations of the Experimental Framework for Experiment 2

One limitation of Experiment 2 is the rather poor measurement signal coherence, which gives insight into how well the piezoelectric actuator and the SLDV response measurements are linearly related. Below around 600 Hz, the coherence is very low, so the FRFs (both coupled and reference) do not carry meaningful information in that range. In other words, at those low frequencies, only a small fraction of the measured response actually comes from the actuator.

Another problem is measurement noise, which affects higher frequencies as well. For the reference, this noise can be filtered out easily – so the residual noise left in the reference FRFs is barely noticeable. However, for the coupled setup, the same filtering does not fully solve the problem. Due to the matrix inversions used in the VPT and LM-FBS methods, the residual noise left after filtering gets amplified. That is why the coupled FRFs often look irregular or “noisy” compared to the smoother reference FRFs.

The key takeaway for this section is that the piezoelectric actuator is largely responsible for the issues described. Although it has several advantages, it is not an ideal source of excitation when used in the current way within the experimental framework of this thesis. It can be expected that a modal hammer would have been a better choice for excitation in terms of noise. This is supported by [3], which shows cleaner coupling results, when using a modal hammer for excitation and an LDV for response measurements.

However, it doesn't necessarily mean the actuator itself is bad – it's possible that the way it was mounted contributed to the poor results at low frequencies: While a reaction mass was added to increase the maximum possible force the actuator can generate [25], a constant preload (e.g., using a casing with spring, see [31]) could have reduced noise and improved excitation quality at lower frequencies.

From a practical standpoint, the piezoelectric actuator is fairly fragile and must be handled with care, especially when re-mounting it often as in Experiment 2. The use of the connector (see Figure 23) helped a lot by making it easier to detach the strong superglue bond from the structure. Nevertheless, attaching and detaching the actuator 16 times was a major factor that increased the overall duration of the experimental procedure.

Another important point is that the usefulness of an SLDV in FBS strongly depends on the structure's geometry. While this was not a major issue in the setup used in this study, it is important to keep in mind generally: the geometry of the interface affects how feasible the VPT is when measuring interface responses with an SLDV. For a 3D VPT (1D in this thesis), at least three interface surfaces (in the x, y, and z directions) need to be accessible to the SLDV – ideally flat and oriented perpendicular to the laser beam. However, not all interfaces have such surfaces. Also, performing a 3D VPT with an SLDV would require a special suspension setup for each measurement direction.

In contrast, accelerometers can be attached directly and measure vibrations in all three directions. Additionally, if parts of the interface are hidden, accelerometers can often be placed nearby, whereas the SLDV needs a clear line of sight to an accessible surface. This may require measuring on a surface further away from the actual VP (which was partly the case for interface measurements for B in this thesis), which might reduce the validity of the FBS rigidity assumption.

6 Conclusion

The conclusion section summarizes the main findings from the previous sections. Additionally, recommendations for future work are provided.

6.1 Summary of Main Findings

As a first attempt at using SLDV for response measurement in FBS, this study yielded promising results. Experiment 1 demonstrated that FBS can perform well when only three DoFs are coupled after being reduced into the VP using a one-dimensional VPT. Consequently, the coherence between the numerically coupled system and the reference was very high (> 0.9) across all examined force-response combinations. Nevertheless, FBS introduced small frequency shifts, likely due to high interface loading in certain modes (which may affect the FBS rigidity assumption) and relative motion resulting from not coupling all DoFs.

The geometry of the AM structure and the choice of which DoFs to couple (especially the direction) are expected to influence the quality of the 1D VPT results. A 1D VPT allows relative interface motion in the DoFs that are not coupled, which can affect the validity of the FBS coupling results. In this study, the geometry of the AM Structure naturally lent itself to investigation in the Z-direction. As a result, translation in Z was coupled directly, while rotations in X and Y were implicitly included due to the planar distribution of interface responses.

Since the number, placement, and orientation of DoFs were carefully defined in Experiment 1 with regard to Experiment 2, Experiment 2 proceeded without major practical issues. In particular, placing the force and response DoFs on opposite sides of the AM structure's main flat surface greatly facilitated the experimental procedure.

The scanning feature of the SLDV allowed for the generation of FRFs with many force-response combinations. Additionally, it enabled the creation of fine-grid mode shapes, which would have required significantly more time using conventional response measurement equipment. Overall, the coupling results (although not as good as numerical), were decent with coherence between the experimentally coupled system and the reference above 0.7 across all examined force-response combinations.

Although the SLDV is highly precise, the measurement signal coherence (especially below 600 Hz) was poor, effectively making results below that frequency unreliable. This issue is linked to the piezoelectric actuator, which proved to be a double-edged sword. On one hand, it was highly valued as a continuous and easily re-mountable excitation source. Given that the SLDV scanning process is not instantaneous and multiple excitation positions were used, these characteristics were particularly beneficial. On the other hand, the actuator exhibited reduced performance at below 600 Hz and introduced noise across the frequency range.

While FRFs at lower frequencies were not particularly meaningful, valuable results were still obtained across most of the frequency range. These findings provide a solid foundation for further improvements, and addressing the identified noise-related issues will be a focus for future research.

6.2 Suggestions for Future Work

The following points outline potential directions for future work based on the findings of this study.

- Attempt FBS coupling of all six DoFs with an SLDV to see if it reduces frequency shifts between the coupled system and the reference (numerical and experimental).
- Apply a constant preload (e.g., using a casing with spring) to the piezoelectric actuator, to assess whether it improves excitation at low frequencies and reduces overall noise.
- Use a different excitation source to address the issues encountered with the piezoelectric actuator (e.g., modal hammer or shaker). Note this may significantly increase experimental time.

7 References

- [1] D. De Klerk, D. J. Rixen, and S. N. Voormeeren, “General framework for dynamic substructuring: History, review, and classification of techniques,” *AIAA Journal*, vol. 46, no. 5, pp. 1169–1181, May 2008.
- [2] M. V. Van Der Seijs, D. D. Van Den Bosch, D. J. Rixen, and D. De Klerk, “An improved methodology for the virtual point transformation of measured frequency response functions in Dynamic Substructuring,” in *ECCOMAS Thematic Conference - COMPDYN 2013*, National Technical University of Athens, 2013, pp. 4334–4347.
- [3] F. Trainotti, T. F. C. Berninger, and D. J. Rixen, “Using Laser Vibrometry for Precise FRF Measurements in Experimental Substructuring,” in *Conference Proceedings of the Society for Experimental Mechanics Series*, Springer New York LLC, 2020, pp. 1–11.
- [4] C. Schedlinski, J. Schell, E. Biegler, and J. Sauer, “Application of optical measurement techniques for experimental modal analyses of lightweight structures,” 2016.
- [5] A. Drozg, G. Čepon, and M. Boltežar, “Full-degrees-of-freedom frequency based substructuring,” *Mech Syst Signal Process*, vol. 98, pp. 570–579, Jan. 2018.
- [6] B. Jetmundsen, R. L. Bielawa, and G. Flannelly, “Generalized Frequency Domain Substructure Synthesis,” *Journal of the American Helicopter Society*, 1988.
- [7] D. De Klerk, D. J. Rixen, and J. De Jong, “The Frequency Based Substructuring Method reformulated according to the Dual Domain Decomposition Method,” in *24th Modal Analysis Conference, St Louis, MO*, Bethel, CT, 2006.
- [8] E. Pagnacco, D. J. Rixen, and T. Godeby, “Dual assembly of substructures and the FBS method: Application to the dynamic testing of a guitar,” 2006.
- [9] M. Van der Seijs, “Experimental Dynamic Substructuring,” PhD Thesis, 2016.

-
- [10] S. W. B. Klaassen, M. V. van der Seijs, and D. de Klerk, “System equivalent model mixing,” *Mech Syst Signal Process*, vol. 105, pp. 90–112, May 2018.
 - [11] “Frequency Based Substructuring — pyFBS documentation.” Accessed: Mar. 07, 2025.[Online].Available:https://pyfbs.readthedocs.io/en/latest/examples/fbs/frequency_based_substructuring.html
 - [12] “Free-Free Modal Analysis – Computational Mechanics.” Accessed: Mar. 30, 2025. [Online]. Available: <https://computationalmechanics.in/free-free-modal-analysis/>?
 - [13] M. Häußler and D. J. Rixen, “Optimal transformation of frequency response functions on interface deformation modes,” in *IMAC 2017 - International Modal Analysis Conference*, Bethel, CT, 2017.
 - [14] M. Brøns, F. Trainotti, and D. J. Rixen, “A novel optimization framework using frequency-based substructuring for estimation of linear bolted joint stiffness and damping,” *Mech Syst Signal Process*, vol. 223, Jan. 2025.
 - [15] A. El Mahmoudi *et al.*, “A Tutorial on an Open-Source Python Package for Frequency-Based Substructuring and Transfer Path Analysis,” in *Conference Proceedings of the Society for Experimental Mechanics Series*, Springer, 2023, pp. 107–117.
 - [16] T. Bregar, A. El Mahmoudi, M. Kodrič, G. Čepon, M. Boltežar, and D. J. Rixen, “Introducing pyFBS: An Open-Source Python Package for Frequency Based Substructuring and Transfer Path Analysis,” in *Conference Proceedings of the Society for Experimental Mechanics Series*, Springer, 2022, pp. 81–89.
 - [17] J. Jung, S. Goo, and J. Kook, “Predicting anti-resonance frequencies using a novel eigenvalue formulation,” *Finite Elements in Analysis and Design*, vol. 191, Sep. 2021.
 - [18] P. Avitabile, “MODAL SPACE-IN OUR OWN LITTLE WORLD,” 2012.

-
- [19] M. Kodrič, G. Čepon, and M. Boltežar, “Experimental framework for identifying inconsistent measurements in frequency-based substructuring,” *Mech Syst Signal Process*, vol. 154, Jun. 2021.
 - [20] H. G. Pasha, R. J. Allemang, and A. W. Phillips, “Techniques for synthesizing FRFs from analytical models,” in *Conference Proceedings of the Society for Experimental Mechanics Series*, Springer New York LLC, 2014, pp. 73–79.
 - [21] P. Avitabile, “MODAL SPACE-IN OUR OWN LITTLE WORLD,” 2007.
 - [22] M. Brøns, “Modified Timoshenko Beam Vibration Theory,” Master Thesis, 2017.
 - [23] M. Brøns and J. J. Thomsen, “Scanning laser Doppler vibrometry,” in *Abstract from 1st International Symposium on Multi-Scale Experimental Mechanics*, Roskilde, 2016.
 - [24] F. Giraud and C. Giraud-Audine, “Introduction,” in *Piezoelectric Actuators: Vector Control Method*, Elsevier, 2019, pp. 1–42.
 - [25] “Dynamic Operation.” Accessed: May 19, 2025. [Online]. Available: <https://www.physikinstrumente.com/en/expertise/technology/piezotechnology/properties-piezo-actuators/dynamic-operation>
 - [26] C. S. Andreasen, J. J. Thomsen, and C. Berggreen, *Experimental Solid Mechanics –Exercise Instructions & Compendium*. Technical University of Denmark - Department of Civil and Mechanical Engineering, 2025.
 - [27] W. D’Ambrogio and A. Fregolent, “The use of antiresonances for robust model updating,” *J Sound Vib*, vol. 236, no. 2, pp. 227–243, Sep. 2000.
 - [28] D. De Klerk and R. J. Visser, “Characterization of Measurement Errors in Experimental Frequency Based Substructuring,” in *Proceedings of ISMA2010*, 2010.
 - [29] H. Zhao, J. Lv, Z. Wang, T. Gao, and W. Xiong, “Finite Element Model Updating Using Resonance–Antiresonant Frequencies with Radial Basis Function Neural Network,” *Applied Sciences (Switzerland)*, vol. 13, no. 12, Jun. 2023.

- [30] M. I. Friswell, A. Chandrashaker, and S. Adhikari, “An Energy Measure for Mode Localization.”
- [31] Y. K. Yong, “Preloading Piezoelectric Stack Actuators in High-Speed Nanopositioning Systems,” Oct. 27, 2016, *Frontiers Media S.A.*
- [32] A. Drozg, J. Rogelj, G. Čepon, and M. Boltežar, “On the performance of direct piezoelectric rotational accelerometers in experimental structural dynamics,” *Measurement (Lond)*, vol. 127, pp. 292–298, Oct. 2018.
- [33] “Wiener filter - Wikipedia.” Accessed: May 12, 2025. [Online]. Available: https://en.wikipedia.org/wiki/Wiener_filter
- [34] S. L. Gjelstrup, “What is Modal Analysis: The Ultimate Guide | Dewesoft.” Accessed: May 17, 2025. [Online]. Available: <https://dewesoft.com/blog/what-is-modal-analysis>